Studying dark matter haloes with weak lensing

Velander, M.B.M.

4 The relation between galaxy dark matter haloes and baryons in the CFHTLS from weak lensing

Velander M., van Uitert E., Hoekstra H. and the CFHTLenS Collaboration, in prep.

Current theories of structure formation predict that galaxies are immersed in extensive dark matter haloes. To learn more about the baryon-dark matter connection it is therefore imperative to probe large scales as well as small. Weak galaxy-galaxy lensing has the power to do this since it not only is sensitive on a large range of scales, but also is independent of the type of matter studied. We present a study of large-scale galaxy dark matter halo properties as a function of the characteristics of the baryonic host galaxies using data from one of the largest completed weak lensing surveys to date, the CFHTLS. Dividing our lens sample into red and blue subsamples, we find that for red galaxies, the halo mass scales with luminosity as $M_{200} \propto L_r^{1.28^{+0.10}_{-0.08}}$ and with stellar mass as $M_{200} \propto M_*^{1.36^{+0.10}_{-0.06}}$, while for blue galaxies $M_{200} \propto L_r^{0.50^{+0.18}_{-0.12}}$ and $M_{200} \propto M_*^{0.54^{+0.06}_{-0.08}}$. We also find indications that blue galaxies reside in less clustered environments than red galaxies do.

4.1 Introduction

In order to fully understand the mechanisms behind galaxy formation, the connection between galaxies and the extensive dark matter haloes in which they are enveloped must be studied in exhaustive detail. In pursuit of this precision, reliable mass estimates of both the baryonic and the dark matter content of galaxies are required. The visible component may be evaluated using e.g. the galaxy luminosity or the stellar mass, which can be derived using stellar synthesis models (Kauffmann et al., 2003; Gallazzi et al., 2005; Bell & de Jong, 2001; Salim et al., 2007). The dark matter, on the other hand, cannot be observed directly but must be examined through the influence it has on its surroundings. At the largest scales reached by haloes, optical tracers such as satellite galaxies are scarce. Furthermore, estimates of halo mass from e.g. satellite galaxy kinematics not only require spectroscopic measurements of a large number of objects, which is unfeasible both in terms of time and from a financial perspective, but they also require the application of the virial theorem and all the associated assumptions. To study any and all galaxies it is therefore desirable to use probes independent of these tracers, and independent of the physical state of the halo, but with the power to explore a large range of scales. These requirements are all satisfied by weak gravitational lensing.

Weak gravitational lensing is fundamentally a consequence of general relativity. As light from distant objects travels through the Universe it is deflected by intervening matter. This deflection causes the distant objects, or *sources*, to appear distorted. In the weak regime the distortion is minute, and only by correlating the shapes of a large number of sources can information about the foreground gravitational field be extracted. There are a handful of different ways of correlating these shapes, each resulting in data about a separate category of matter accumulation. By correlating the shape of sources with those of other sources, finely detailed large-scale structure can be discerned in the foreground. The precise properties of this pattern are intimately connected with the composition of our Universe and thus allows for constraints on cosmological parameters via *cosmic shear* (see e.g. Van Waerbeke & Mellier (2003); Hoekstra & Jain (2008); Munshi et al. (2008), for reviews, and e.g. Schrabback et al. (2010) for recent results). Alternatively, source shapes may be correlated with the positions of foreground objects, or *lenses*, through a technique known as *galaxy-galaxy lensing*. The strength of the lensing signal as a function of the distance from the lens holds information on the depth and shape of the potential well causing the distortion. Thus density profiles of the dark matter haloes surrounding galaxies and, equivalently, galaxy clusters may be directly investigated. Simulations predict that dark matter haloes are well approximated by Navarro-Frenk-White profiles (Navarro, Frenk, & White, 1996) and confirming this would provide evidence for the concordance model of cosmology.

Generally, however, galaxies and their haloes are not isolated but reside in clustered environments. The ramification is that the interpretation of the observed galaxy-galaxy lensing signal becomes more complicated since the signal from nearby haloes influence the result. Over the past decade a new approach has gained traction: the weak lensing halo model (e.g. Cooray & Sheth, 2002; Guzik & Seljak, 2002; Mandelbaum et al., 2005; van Uitert et al., 2011; Leauthaud et al., 2011). Within the halo model framework, all haloes are represented

as distinct entities, each with a galaxy at the center. Enclosed in each main halo are satellite galaxies surrounded by subhaloes. In this work we seek to employ the halo model to gain a more accurate picture of galaxy-size dark matter haloes, allowing for a more precise analysis of the link between galaxies and the dark matter haloes they reside in. For this purpose we use data from the Canada-France-Hawaii Telescope Legacy Survey (CFHTLS). The CFHTLS consists of just over 170 deg^2 of images in five filters ($u^*g'r'i'z'$) to the impressive depth of $i' = 24.5$. The CFHTLS weak lensing collaboration (CFHTLenS) has extracted 8.7×10^6 galaxy shears, and provided all objects with reliable photometric redshifts, making this survey one of the most powerful completed weak lensing surveys to date. This work thus improves on the preliminary galaxy-galaxy lensing analysis carried out using a small subset of the CFHTLS data and a single-halo model fit to the inner regions only (Parker et al., 2007).

This Chapter is organised as follows: we introduce the data in Section 4.2. In Section 4.3 we review our halo model and the formalism behind it, and in Section 4.4 we test our shear catalogue for systematic effects. We investigate the lensing signal as a function of luminosity in Section 4.5 and as a function of stellar mass in Section 4.6, and we conclude in Section 4.7. The following cosmology is assumed throughout (WMAP7; Komatsu et al., 2010): $(\Omega_M, \Omega_\Lambda, h, \sigma_8, w) = (0.27, 0.73, 0.70, 0.81, -1)$

4.2 Data

In this Chapter we present a weak lensing analysis of the entire Wide Synoptic Survey of the Canada-France-Hawaii Telescope Legacy Survey (CFHTLS-Wide). The impressive expanse and depth of this survey makes it ideal for weak lensing analyses, as we will show. The CFHTLS is a joint 5-year project between Canada and France which commenced in 2003 and which is now completed. The data are imaged using the Megaprime wide field imager mounted at the prime focus of the Canada-France-Hawaii Telescope (CFHT) and equipped with the MegaCam camera. MegaCam comprises an array of 9×4 CCDs and has a field of view of 1 deg^2. The wide synoptic survey covers an effective area of about 155 deg^2 in five bands: u^*, g', r', i' and z'. This area is composed of four independent fields, W1–4, each with an area of 25-72 deg^2 and with a full multi-colour depth of $i' = 24.7$ (7σ detected source in the CFHTLenS[1] catalogue). The images have been independently reduced within the CFHTLenS Collaboration, and for details on this data reduction process, please refer to Erben et al (in prep.).

4.2.1 Lens sample

The depth of the CFHTLS enables us to investigate lenses with a large range of lens properties and redshifts, which in turn grants us the opportunity to thoroughly study the evolution of galaxy-sized dark matter haloes. An initial study was performed by van Uitert et al. (2011) (hereafter VU11) using the same halo model as the one used here, described in Section 4.3.2. That study exploited a 300 deg^2 overlap between two major lensing surveys. The foreground sample consisted of galaxies from the seventh data release of the Sloan Digital Sky

[1] `http://cfhtlens.org`

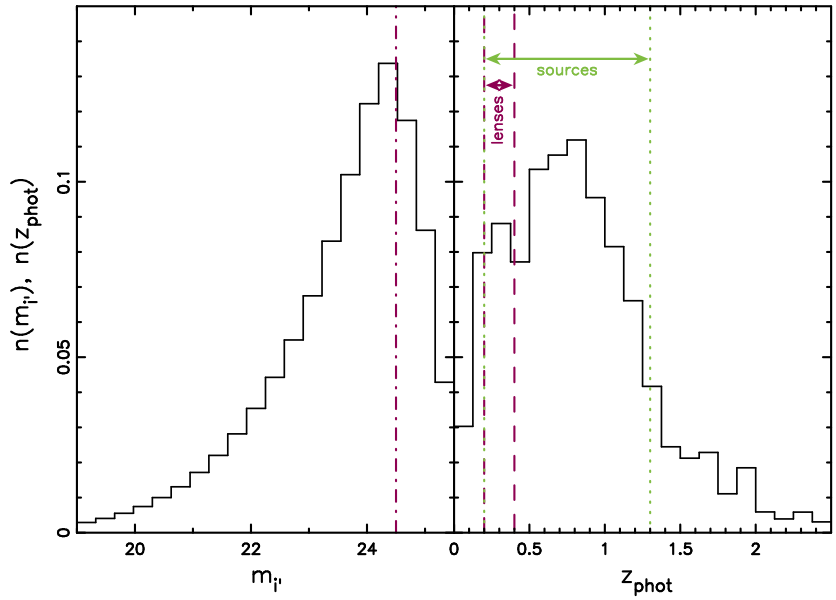

Figure 4.1 Magnitude (left panel) and photometric redshift (right panel) distributions of all objects in the CFHTLenS catalogue, with our lens (source) redshift selection marked with purple dashed (green dotted) lines. Also shown is the cutoff-point in magnitude for all objects used in our analysis (purple dash-dotted).

Survey (SDSS DR7; Abazajian et al., 2009), and objects from the intermediate-depth Second Red Sequence Cluster Survey (RCS2; Gilbank et al., 2011) were used as background sources, improving greatly on previous analyses based on the shallow SDSS alone. However, while their lenses had accurate spectroscopic redshift estimates, their sources did not have enough photometric data available at the time to provide redshift estimates for the sources. Thus the CFHTLS has, aside from the increased depth, a further advantage over the VU11 analysis owing to the high-precision photometric redshifts available for all objects used in our analysis.

Throughout this Chapter, we place an upper cut in apparent magnitude of $i' \leq 24.5$ and select our lenses in redshift such that $0.2 \leq z_{\rm lens} \leq 0.4$, unless explicitly stated otherwise. These selections are illustrated in Figure 4.1. For the full CFHTLS-Wide we achieve a lens count of $N_{\rm lens} = 1.53 \times 10^6$, nearly a hundred times the size of the lens sample used in VU11. We then further split our lens sample in luminosity or stellar mass bins as described in Sections 4.5 and 4.6 to investigate the halo mass trends as a function of lens properties.

4.2.2 Source catalogue

The shear estimates for the sources used in this Chapter have been obtained using LENSFIT as detailed in Miller et al (in prep.), and thoroughly tested by the CFHTLenS Collaboration. During the testing process, the LENSFIT shears were compared to those extracted using other shape measurement methods (such as those introduced in Hoekstra et al., 1998; Kuijken, 2006; Schrabback et al.,

2007; Velander et al., 2011) to successfully eliminate software-specific issues. All sources also have multi-band photometric redshift estimates as described in Hildebrandt et al. (2012).

To ensure photometric accuracy, we use only sources with redshifts of $z_{\rm lens} \leq z_{\rm source} \leq 1.3$, and we impose the same cut in magnitude as we do for the lenses: $i' \leq 24.5$. Furthermore, we ensure that our sources have been detected in at least six exposures. Our source count for the full CFHTLS-Wide (excluding masked areas) is then $N_{\rm source} = 3.9 \times 10^6$, corresponding to a source density of 9.3 arcmin^{-2} which is a factor of 1.5 greater than that of the RCS2.

4.3 Method

To analyse the dark matter haloes in the CFHTLS we use a method known as weak galaxy-galaxy lensing, and compare the measured signal with a halo model. In this section we will introduce the basic formalism and give an overview of our halo model.

4.3.1 Weak galaxy-galaxy lensing

Weak gravitational lensing is the measure of weak distortions induced by foreground structure on background source galaxies. By correlating the shapes of background galaxies, statistical properties of the matter in the foreground can be inferred.

The first-order lensing distortion, shear, is a stretch in one direction which is applied to the intrinsic shape of a source galaxy. By averaging over enough randomly oriented sources we can assume the mean intrinsic galaxy to be circular, and thus any distortion measured is due to lensing. In this analysis we use galaxy-galaxy lensing where source galaxy distortions are averaged in concentric rings centered on lens galaxies. We measure the tangential shear as a function of radial distance from the lens this way, and also the cross shear which is a 45deg rotated signal. The cross shear can never be induced by a lens which means that it may be used as a systematics check. The amplitude of the tangential shear is directly related to the differential surface density $\Delta\Sigma(r)$ via

$$\Delta\Sigma(r) = \Sigma_{\rm crit}\langle\gamma_t(r)\rangle \tag{4.1}$$

where $\Sigma_{\rm crit}$ is the critical surface density

$$\Sigma_{\rm crit} = \frac{c^2}{4\pi G}\frac{D_s}{D_l D_{ls}} \tag{4.2}$$

with D_s, D_l and D_{ls} the angular diameter distance to the source, to the lens and between the lens and source respectively. By using differential surface densities rather than tangential shears, the geometric factor is neutralised and the amplitude of the signals can be directly compared between different samples. The only caveat is that the properties of lenses depend on the lens redshift so this difference still has to be taken into account.

The circular average makes this type of analysis robust against small-scale systematics introduced by e.g. the telescope. None the less, there will be large-scale systematics present, mainly due to areas being masked. By masking areas,

or by considering lenses close to the edge of the area covered, the circular average is in fact not perfectly circular. This effect, most noticeable on large scales, is important to correct for, particularly in the case of precision galaxy-galaxy lensing such as the analysis in this Chapter. Our correction is done by measuring the signal around random lens positions. Were there no systematics present the measured signal would be zero. If it is not, it can easily be corrected for by subtracting it from the observed lensing signal.

As for any concerns regarding the fidelity of the photometric redshifts, the weights we employ use the geometric lensing efficiency $D_s/(D_l D_{ls})$ to down-weight close pairs as described in e.g. Velander et al. (2011) (Chapter 3 of this Thesis), effectively minimising any influence of redshift inaccuracies on the measured signal. Additionally we calculate a correction factor based on the redshift error distribution for each mass estimate to remove any remaining redshift systematics. This calculation is described further in Section 4.5.1.

4.3.2 The halo model

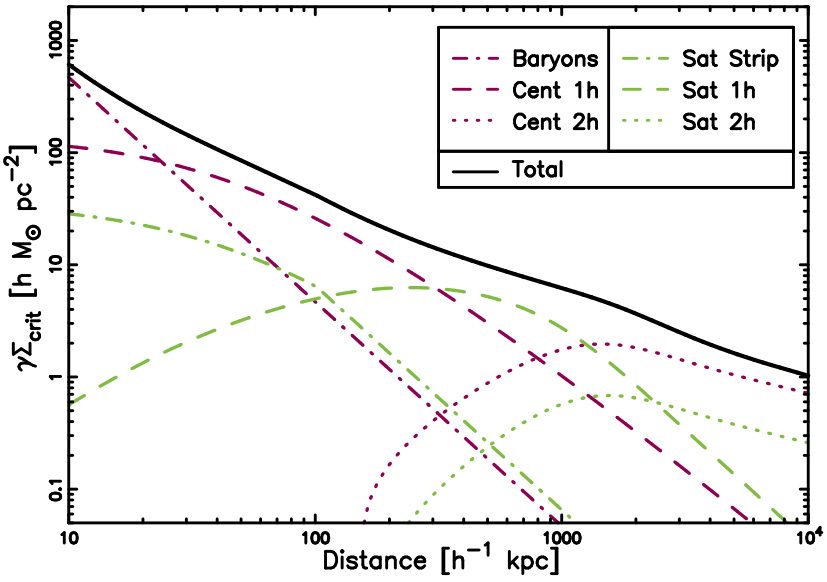

Figure 4.2 Illustration of the halo model used in this Chapter. Here we have used a halo mass of $M_{200} = 10^{12}\ h^{-1}\ M_\odot$, a stellar mass of $M_* = 3 \times 10^{11}\ M_\odot$ and a satellite fraction of $\alpha = 0.2$. The lens redshift is $z_{\rm lens} = 0.5$. Purple lines represent quantities tied to galaxies which are centrally located in their haloes while green lines correspond to satellite quantities. The purple dash-dotted line is the baryonic component, the green dash-dotted line is the stripped satellite halo, dashed lines are the 1-halo components induced by the main dark matter halo and dotted lines are the 2-halo components originating from nearby haloes.

To accurately model the weak lensing signal observed around galaxy-size haloes, we have to account for the fact that galaxies generally reside in clustered environments. In this work we do this by employing the halo model software first introduced in VU11. For full details on the exact implementation, please

see VU11; here we give a qualitative overview.

Our halo model builds on work presented in Guzik & Seljak (2002) and Mandelbaum et al. (2005), where the full lensing signal is modelled by accounting for the central galaxies and their satellites separately. Here we assume that a fraction $(1-\alpha)$ of our galaxy sample reside at the centre of a dark matter halo, and the remaining objects are satellite galaxies surrounded by subhaloes which in turn reside inside a larger halo. In this context α is the *satellite fraction* of a given sample.

The lensing signal induced by central galaxies consists of two components: the signal arising from the main halo (the *1-halo* term $\Delta\Sigma^{\rm 1h}$) and the contribution from neighbouring haloes (the *2-halo* term $\Delta\Sigma^{\rm 2h}$). The two components simply add to give the lensing signal due to central galaxies:

$$\Delta\Sigma_{\rm cent} = \Delta\Sigma^{\rm 1h}_{\rm cent} + \Delta\Sigma^{\rm 2h}_{\rm cent} \tag{4.3}$$

In our model we assume that all main dark matter haloes are well represented by a Navarro-Frenk-White density profile (NFW; Navarro, Frenk, & White, 1996) with a mass-concentration relationship as given by Duffy et al. (2008).

We assume that satellite galaxies reside in subhaloes which have been tidally stripped of dark matter in the outer regions. Adopting a truncated NFW profile which has been stripped of about 50% of its dark matter, we acquire a satellite term which supplies signal on small scales. Thus satellite galaxies add three further components to the total lensing signal: the contribution from the stripped subhalo ($\Delta\Sigma^{\rm strip}$), the satellite 1-halo term which is off-centred since the satellite galaxy is not at the centre of the main halo, and the 2-halo term from nearby haloes. Just as for the central galaxies, the three terms add to give the satellite lensing signal:

$$\Delta\Sigma_{\rm sat} = \Delta\Sigma^{\rm strip}_{\rm sat} + \Delta\Sigma^{\rm 1h}_{\rm sat} + \Delta\Sigma^{\rm 2h}_{\rm sat} \tag{4.4}$$

There is an additional contribution to the lensing signal, not yet considered in the above equations. This is the signal induced by the lens baryons ($\Delta\Sigma^{\rm bar}$). This last term is a refinement to the halo model presented in VU11, necessary since weak lensing measures the total mass of a system and not just the dark matter mass. The baryonic component is modelled as a point source with a mass equal to the mean stellar mass of the lenses in the sample (as in e.g. Leauthaud et al., 2011):

$$\Delta\Sigma^{\rm bar} = \frac{\langle M_* \rangle}{\pi r^2} \tag{4.5}$$

where r is the physical distance from the lens. This term could technically be decomposed into a central and a satellite component. In this work we do not leave the baryon term as a free variable and so we do not need to distinguish between the two. Thus we treat this term as a single entity.

Finally, to obtain the total lensing signal of a galaxy sample of which a fraction α are satellites we combine the baryon, central and satellite galaxy signals, applying the appropriate proportions:

$$\Delta\Sigma = \Delta\Sigma^{\rm bar} + (1-\alpha)\Delta\Sigma_{\rm cent} + \alpha\Delta\Sigma_{\rm sat} \tag{4.6}$$

All components of our halo model are illustrated in Figure 4.2. In this example the halo mass is $M_{200} = 1 \times 10^{12}\ h^{-1} M_\odot$, the stellar mass is $M_* =$

$3 \times 10^{11}\ M_{\odot}$, the satellite fraction is $\alpha = 0.2$, the lens redshift is $z_{\rm lens} = 0.5$ and $D_{ls}/D_s = 0.5$. On small scales the baryonic component is prominent, while on large scales the 2-halo components dominate.

4.4 Systematics tests

4.4.1 Verification of the shear catalogue

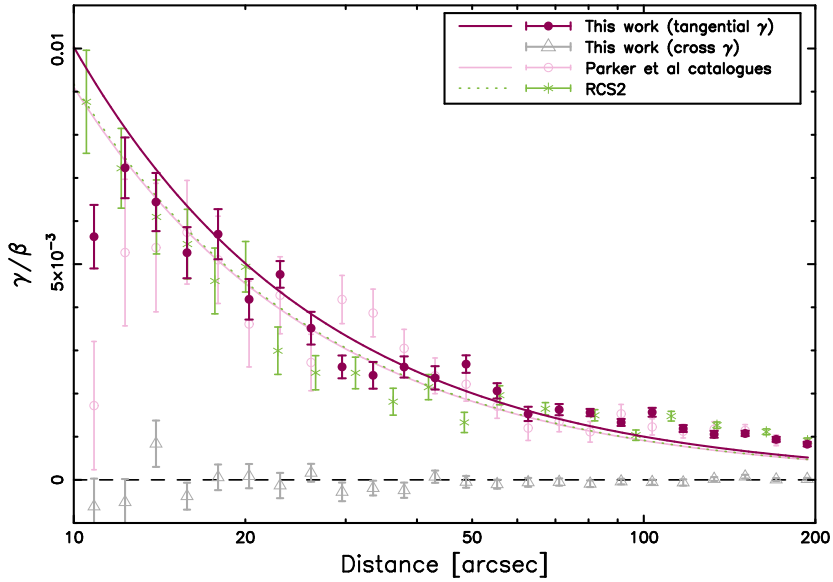

Figure 4.3 Comparison of three data sets: the KSB catalogues from ~ 22 deg^2 CFHTLS (pink circles), the results from RCS2 (green stars) and our results (purple dots). The lines show the best fit singular isothermal sphere for each dataset (with green and pink nearly identical), and the grey triangles show the cross-shear from our results which should be zero in the absence of systematic errors.

In this study we use lenses and sources from the 155 deg^2 CFHTLS, with high-quality photometric data and redshifts available for all objects. To validate the quality of our shear catalogue we compare with the results from two previous analyses of a very similar nature. The first is a preliminary weak galaxy-galaxy lensing analysis of the CFHTLS-Wide conducted by Parker et al. (2007). At that time, the survey was not yet finished, so they only had access to an area of ~ 22 deg^2 in i'-band corresponding to about 15% of our area. Since they only had data from one band their analysis also lacked redshift estimates for lenses and sources, but they separated lenses from sources using magnitude cuts. They then obtained shear estimates for their sources using a version of the technique introduced by Kaiser, Squires, & Broadhurst (1995) as outlined in Hoekstra et al. (1998). For their average lens they derived a best-fit velocity dispersion of $\sigma_v = 132 \pm 10$ km s^{-1} using a singular isothermal sphere profile (SIS) to model the lensing signal, though there is some disagreement between this number and our findings (see discussion below). The second analysis is based on the shear

Table 4.1 Details of the seeing bins.

Sample	$N_{\rm fields}$	$\langle r_* \rangle$ [arcsec]	θ_E [arcsec]	σ_{θ_E}
P1	27	0.50	0.053	0.005
P2	23	0.57	0.044	0.006
P3	33	0.62	0.050	0.005
P4	38	0.67	0.047	0.005
P5	28	0.72	0.040	0.006
P6	36	0.80	0.049	0.005

catalogue from VU11 (see Section 4.2). The data used in that study is from the RCS2 which is slightly shallower than the CFHTLS and for which no redshifts were available for the sources at the time of this analysis.

To compare and contrast our lensing signal with the one obtained by Parker et al. (2007) we apply the same i'-band magnitude cuts as they did, viz. $19.0 < i' < 22.0$ for lenses and $22.5 < i' < 24.5$ for sources. A slight difference between their analysis and ours is that Parker et al. (2007) boosts their signal by an approximate factor to correct for contamination by sources that are in front of, or physically associated with, the lens while we use our redshift information to minimise this contamination. The resulting galaxy-galaxy signal, scaled with the angular diameter distance ratio $\beta = D_{ls}/D_s = 0.67$, is shown as purple dots in Figure 4.3. The best-fit SIS profile corresponds to a velocity dispersion of $\sigma_v = 83.3 \pm 1.6$ km s^{-1}, which is somewhat lower than the one quoted in Parker et al. (2007). However, we re-analysed the actual shear catalogues used for the Parker et al. (2007) analysis and the results are shown as light circles in Figure 4.3. For that signal, which is corrected for contamination using the Parker et al. (2007) boost factor, we find a velocity dispersion of $\sigma_v = 79.4 \pm 3.3$ km s^{-1} using the redshifts stated in Parker et al. (2007). This is in good agreement with our analysis of the full CFHTLS-Wide. The discrepancy with the velocity dispersion quoted in Parker et al. (2007) remains unexplained, but we have shown that the shear estimates are consistent between the two CFHTLS catalogues.

Furthermore, also shown as green stars in Figure 4.3 is the signal obtained by VU11 using RCS2 and the same magnitude selection as Parker et al. (2007). The shears have been corrected for contamination by physically associated sources, as described in VU11, and scaled with the $\beta = 0.48$ appropriate for the RCS2. For this signal we find a velocity dispersion of $\sigma_v = 79.7 \pm 2.3$ km s^{-1} which is again in good agreement with our results. Based on this, and based on our re-analysis of the original Parker et al. (2007) shear catalogues, we conclude that our shear estimates are valid and reliable for further galaxy-galaxy lensing studies.

4.4.2 Seeing test

In general a round PSF causes circularisation of source images which in turn causes a multiplicative bias of the shapes measured. The amount of bias depends on the size of the PSF. Assuming that the shapes of very well resolved galaxies

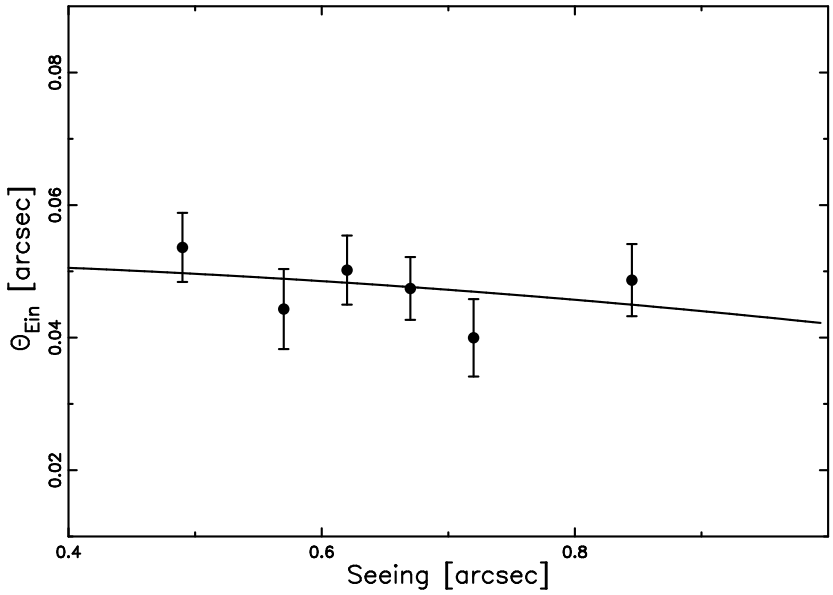

Figure 4.4 The weak galaxy-galaxy signal measured in each of 6 seeing bins, according to Table 4.1.

can be accurately recovered we can model the effect of the PSF as

$$\gamma^{\rm obs} = \gamma^{\rm true}\left[1 + \mathcal{M}\left(\frac{r_*}{r_0}\right)^2\right] \tag{4.7}$$

where $\gamma^{\rm obs}$ is the observed shear, $\gamma^{\rm true}$ is the true shear, r_* is the PSF size and r_0 is the intrinsic (Gaussian) size of the galaxy. The particular dependence on PSF size is the result of a full moments analysis. $\mathcal{M}$ is a function close to zero representing the multiplicative bias and may be separated into two components:

$$\mathcal{M} = \mathcal{M}' + \mathcal{P} \tag{4.8}$$

where $\mathcal{M}'$ is the true limitation of the shape measurement method and $\mathcal{P}$ is the bias contribution induced by the PSF. This last term depends on the statistical and systematic errors in the size estimates. Thus if the shape measurement software has no intrinsic bias and if the PSF is perfectly known, then the dominant source of shear bias is the accuracy of the size estimates of the faint, small galaxies. For the Bayesian shape measurement method used in this Chapter, LENSFIT, this term will be negligible.

This multiplicative bias may be related to the parameterisation used in the Shear Testing Programme (STEP Heymans et al., 2006a; Massey et al., 2007a), $m_{\rm STEP}$, via

$$m_{\rm STEP} = \mathcal{M}\left\langle\left(\frac{r_*}{r_0}\right)^2\right\rangle \tag{4.9}$$

The smallest bias achieved by the pipelines taking part in STEP was $m_{\rm STEP} \sim 0.01$ which, for the adopted size distribution and simulated ground-based data used in STEP, corresponds to $\mathcal{M} \sim 0.005$.

Since the bias depends on the size of the PSF, data with a spread in seeing should enable us to determine the bias $\mathcal{M}$ directly from the data, thus allowing us to deduce the true performance of the shape measurement pipeline. The CFHTLS has such a spread, with the best seeing being 0.44 arcsec and the worst being 0.94 arcsec.

Galaxy-galaxy lensing provides us with a neat way of determining the bias. Assuming that the systematic offset due to PSF anisotropy is negligible (a fair assumption given our correction for spurious signal around random lenses; see Section 4.3.1) the observed shear is related to the true shear via

$$\gamma^{\rm obs} = (1 + m_{\rm STEP})\gamma^{\rm true} \tag{4.10}$$

For a singular isothermal sphere (SIS), the amplitude of the shear signal as a function of distance θ from the lens is

$$\gamma(\theta) = \frac{\theta_E}{2\theta} \tag{4.11}$$

where θ_E is the Einstein radius. Thus there is a simple relationship between the observed Einstein radius and the true one:

$$\theta_E^{\rm obs} = \left(1 + \mathcal{M}\left\langle\left(\frac{r_*}{r_0}\right)^2\right\rangle\right)\theta_E^{\rm true} \tag{4.12}$$

By measuring the Einstein radius of the average lens as a function of seeing we can therefore determine both the true Einstein radius and the performance of the shape measurement pipeline.

We split the data according to Table 4.1, measure the galaxy-galaxy lensing signal in each seeing bin and fit an SIS to the innermost 140 h^{-1} kpc. By fitting only small scales we avoid the influence of neighbouring haloes. The results are shown in Figure 4.4 and quoted in Table 4.1. We then fit the relation described by Equation 4.12 to the resulting Einstein radii and find a value of $\mathcal{M} = -0.048 \pm 0.071$ which implies a STEP bias of $m_{\rm STEP} = -0.094 \pm 0.14$. This is consistent with no bias given the error bars, but with a greater range in seeing we would be able to constrain this bias even further. According to this analysis, the true Einstein radius of the average lens galaxy in our sample is $\theta_E^{\rm true} = 0.052" \pm 0.007"$.

4.5 Luminosity trend

The luminosity of a galaxy is an easily obtainable indicator of its baryonic content. To investigate the relation between dark matter halo mass and galaxy mass we therefore split the lenses into 8 bins according to MegaCam r'-band magnitudes as detailed in Table 4.2 and illustrated in Figure 4.5. The choice of bin limits follow the lens selection in VU11, a previous analysis carried out using the shallower RCS2 and an earlier version of the halo model we use here. This choice will allow us to compare our results to the results obtained by VU11 because the RCS2 data have been obtained using the same filters and telescope. Since the behaviour of early-type galaxies is expected to differ from that of late-type galaxies, using only one luminosity estimate to characterise a lens sample results in an average relation which may be difficult to interpret.

Table 4.2 Details of the luminosity bins. (1) Absolute magnitude range; (2) Number of lenses; (3) Mean redshift; (4) Fraction of lenses that are blue; (5) Mean luminosity for red lenses [10^{10} $L_\odot$]; (6) Mean stellar mass for red lenses [10^{10} $M_\odot$]; (7) Redshift-corrected best-fit halo mass for red lenses [10^{11} h^{-1} $M_\odot$]; (8) Best-fit satellite fraction for red lenses; (9) Mean luminosity for blue lenses [10^{10} $L_\odot$]; (10) Mean stellar mass for blue lenses [10^{10} $M_\odot$]; (11) Redshift-corrected best-fit halo mass for blue lenses [10^{11} h^{-1} $M_\odot$]; (12) Best-fit satellite fraction for blue lenses

Sample	$M_r{}^{(1)}$	$n_{\rm lens}{}^{(2)}$	$\langle z\rangle^{(3)}$	$f_{\rm blue}{}^{(4)}$	$\langle L_r^{\rm red}\rangle^{(5)}$	$\langle M_*^{\rm red}\rangle^{(6)}$	$M_h^{\rm red(7)}$	$\alpha^{\rm red(8)}$	$\langle L_r^{\rm blue}\rangle^{(9)}$	$\langle M_*^{\rm blue}\rangle^{(10)}$	$M_h^{\rm blue(11)}$	$\alpha^{\rm blue(12)}$
L1	[-21.0,-20.0]	89215	0.30	0.61	0.91	4.72	$2.36^{+0.68}_{-0.53}$	$0.30^{+0.02}_{-0.02}$	0.83	2.48	$0.87^{+0.57}_{-0.35}$	$0.00^{+0.01}_{-0.00}$
L2	[-21.5,-21.0]	31889	0.30	0.40	1.76	8.97	$4.39^{+1.40}_{-1.06}$	$0.20^{+0.03}_{-0.02}$	1.71	5.12	$1.78^{+1.18}_{-0.71}$	$0.00^{+0.03}_{-0.00}$
L3	[-22.0,-21.5]	22492	0.30	0.29	2.77	14.1	$4.55^{+1.45}_{-1.10}$	$0.24^{+0.03}_{-0.03}$	2.71	8.16	$3.39^{+2.50}_{-1.44}$	$0.00^{+0.02}_{-0.00}$
L4	[-22.5,-22.0]	13105	0.30	0.21	4.32	22.1	$10.4^{+3.30}_{-2.50}$	$0.20^{+0.03}_{-0.03}$	4.28	12.9	$0.87^{+1.53}_{-0.82}$	$0.13^{+0.06}_{-0.06}$
L5	[-23.0,-22.5]	5840	0.30	0.15	6.75	34.6	$17.5^{+5.58}_{-4.23}$	$0.22^{+0.04}_{-0.04}$	6.71	20.2	$0.53^{+2.60}_{-0.52}$	$0.04^{+0.10}_{-0.10}$
L6	[-23.5,-23.0]	1769	0.29	0.12	10.5	53.8	$39.4^{+13.7}_{-10.2}$	$0.17^{+0.06}_{-0.06}$	10.8	32.0	$0.99^{+6.50}_{-0.98}$	$0.27^{+0.22}_{-0.22}$
L7	[-24.0,-23.5]	389	0.29	0.16	16.5	84.0	$132^{+46.1}_{-34.2}$	$0.01^{+0.11}_{-0.11}$	17.3	49.7	$0.01^{+6.04}_{-0.00}$	$0.00^{+0.18}_{-0.00}$
L8	[-24.5,-24.0]	87	0.27	0.24	25.8	132	$167^{+137}_{-75.2}$	$0.38^{+0.26}_{-0.26}$	29.6	84.2	$7.48^{+31.8}_{-7.47}$	$0.00^{+0.25}_{-0.00}$

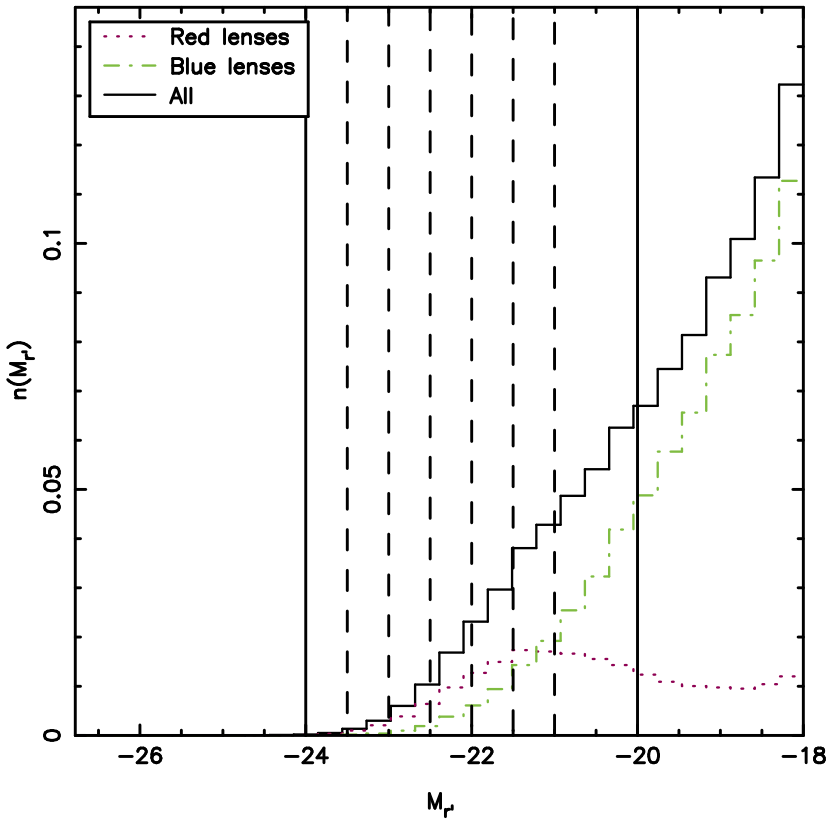

Figure 4.5 r'-band absolute magnitude distribution in the CFHTLS for lenses with redshifts $0.2 \leq z_{\rm lens} \leq 0.4$ (black solid histogram). The distribution of red (blue) lenses is shown in dotted purple (dot-dashed green). Our lens bins are marked with vertical lines.

Since we have access to multi-colour data, we are able to further divide our lenses in each bin into a red and a blue sample, approximately corresponding to early-type and late-type galaxies. In practice we do this using their photometric types $T_{\rm BPZ}$. $T_{\rm BPZ}$ is a number in the range of $[1.0, 6.0]$ representing the best-fit spectral energy distribution (SED) and we define our red and blue samples as galaxies with $T_{\rm BPZ} < 1.5$ and $T_{\rm BPZ} > 2.0$ respectively where the latter captures most spiral galaxies. A colour-colour comparison confirms that these samples are well defined. We proceed to measure the galaxy-galaxy lensing signal for each sample, and fitting it with our halo model, leaving the halo mass M_{200} and the satellite fraction α as free parameters. The results are shown in Figure 4.6 for all luminosity bins and for each red and blue lens sample, with details of the fitted halo model parameters quoted in Table 4.2. Qualitatively comparing these results to the ones presented in VU11 we see that the amplitudes of the signals agree well.

An overview of the broad trends in Figure 4.6 is given in Figure 4.7 for red galaxies and Figure 4.8 for blue. As expected, the amplitude of the signal increases with luminosity for both red and blue samples indicating an increased

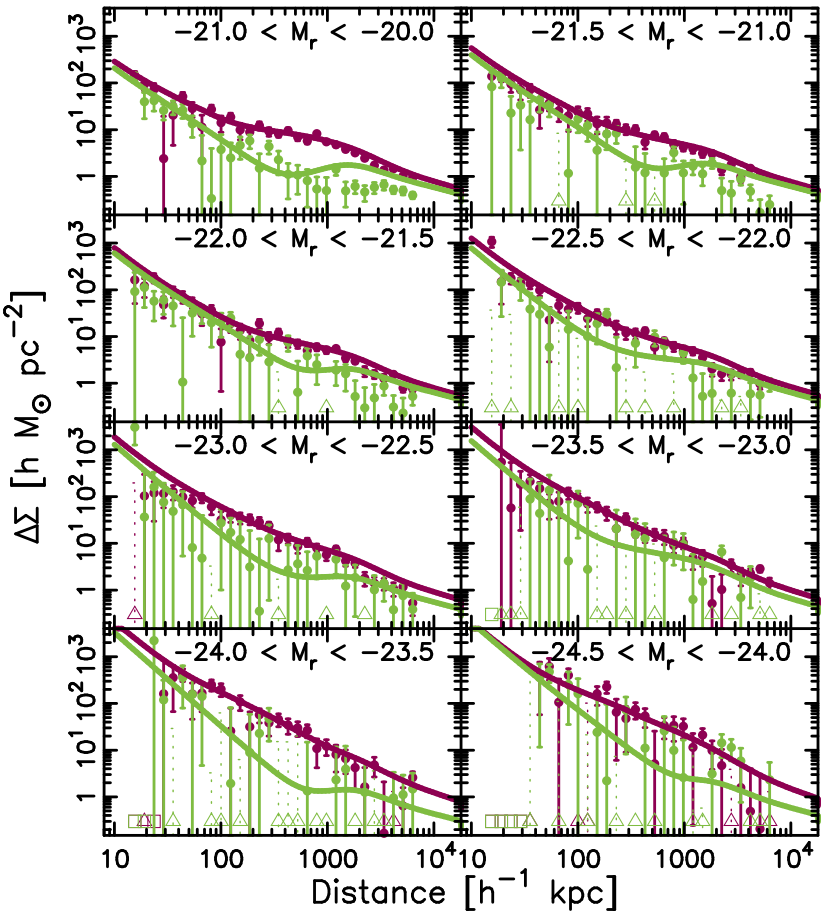

Figure 4.6 The weak galaxy-galaxy signal around lenses which have been split into luminosity bins according to Table 4.2, modelled using the halo model described in Section 4.3.2. The purple (green) dots represent the measured differential surface density of the red (blue) lenses, and the solid line is the best-fit halo model. Triangles represent negative points that are included unaltered in the model fitting procedure, but that have here been moved up to positive values as a reference. The dotted error bars are the unaltered error bars belonging to the negative points. The squares represent distance bins containing no objects. For a detailed decomposition into the halo model components, please refer to Appendix 4.A.

halo mass. In general, for identical luminosity selections blue galaxies have less massive haloes than red do. For the red sample, lower luminosity bins display a slight bump at scales of $\sim 0.5\ h^{-1}$ Mpc. This is due to the satellite 1-halo term becoming significant and indicates that a large fraction of the galaxies in those bins are in fact satellite galaxies inside a larger halo. Thus brighter galaxies are more likely to be centrally located in a halo. The blue galaxies also display a bump for the lower luminosity bins, but this feature is at larger scales than the satellite 1-halo term. The signal breakdown shown in Figure 4.20 (Appendix 4.A) reveals that this bump is due to the central two-halo term, i.e. it

is the contribution from nearby haloes.

To make a quantitative comparison with VU11, however, there are several differences between the analyses that have to be taken into account. Firstly, including the baryonic component in our halo model results in a lower halo mass estimate than not doing so (see Section 4.5.2 and Figure 4.12 for a more extensive discussion on this topic). This is intuitive since gravitational lensing measures the total mass of a system and we are allowing some of that mass to be baryonic, leaving less mass for the dark matter halo. Secondly, the red and blue selection in our analysis does not necessarily correspond to the early- and late-type classification in VU11, making a completely fair comparison difficult. Thirdly, we have a strong enough signal to be able to limit our lens sample to a small redshift range, which minimises any contamination of the relations due to redshift evolution. Finally, we do not have spectroscopic redshifts for our lenses which means that our lenses may have been assigned an inaccurate redshift. This will cause a luminosity-dependent bias in the halo mass estimate, as discussed in e.g. Hoekstra et al. (2005). We will examine this effect further in the next Section.

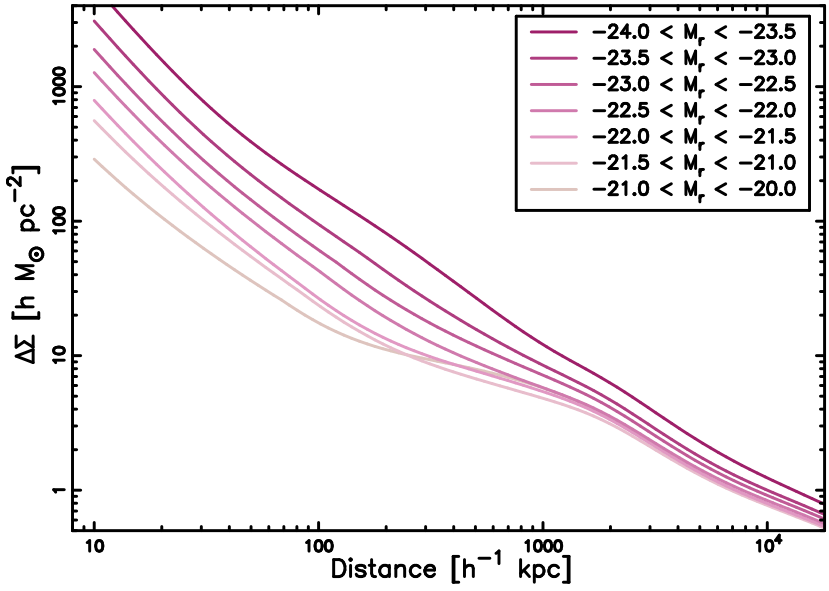

Figure 4.7 Best-fit halo models for red lenses for all luminosity bins.

4.5.1 Photometric redshift error corrections

Before interpreting the luminosity results we have to take into account the redshift bias effect previously mentioned. The accuracy of our photometric redshifts is high, but never the less the errors on the redshift estimates have to be taken into account. If the true redshift differs from the estimated one, this will affect all derived quantities. An underestimated redshift, for example, would cause the estimated absolute magnitude to be fainter than the true absolute magnitude and the lens would be placed in the wrong luminosity bin. As can be seen in Fig-

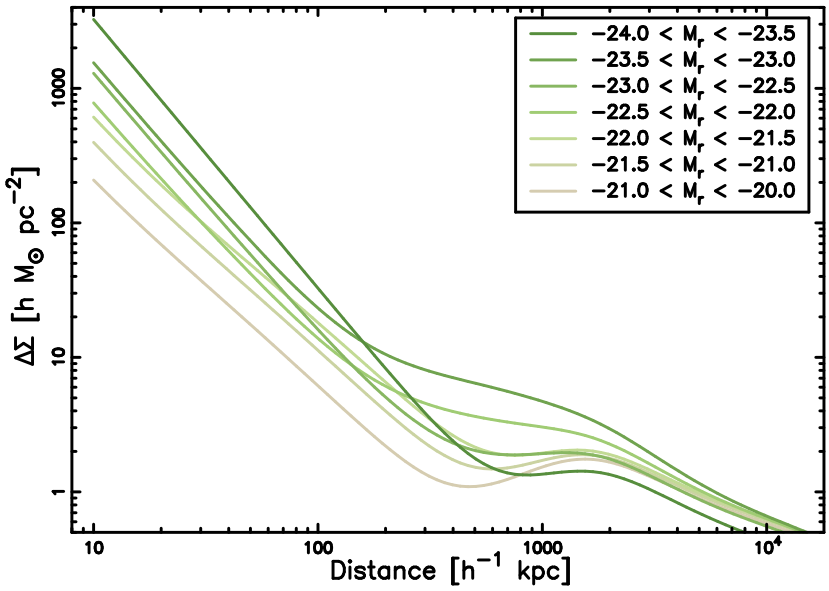

Figure 4.8 Best-fit halo models for blue lenses for all luminosity bins.

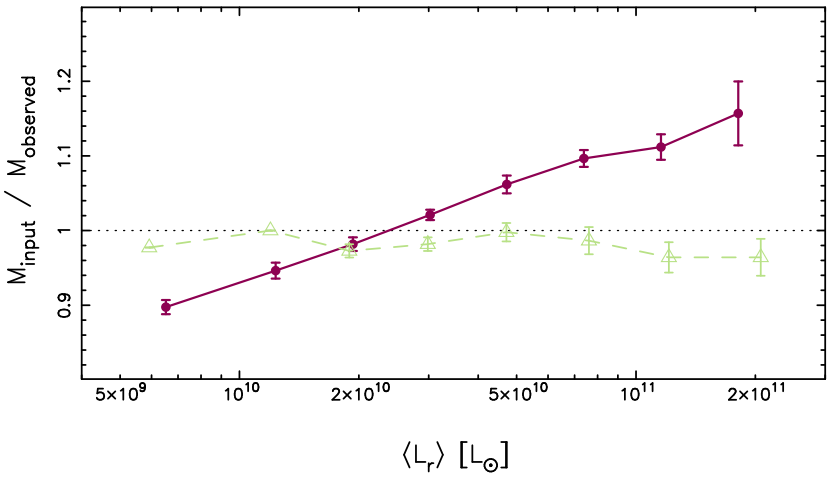

Figure 4.9 Bias as a function of luminosity induced through inaccuracies in the photometric redshift estimates. The purple solid (green dashed) line with dots (triangles) shows the bias for the red (blue) lens sample. The error bars are obtained using ten lens catalogue realisations.

ure 4.5 there are more faint objects than bright, which means that more objects will scatter from fainter bins into brighter bins than the other way around. This will lower the lensing signal in each bin and bias the observed halo mass low, and the amount of bias will be luminosity dependent. To estimate the impact of this bias we create a simulated version of the CFHTLS-Wide as follows. We fit an initial powerlaw mass-luminosity relation of the form $M_{200} = M_{0,L}(L/L_{\rm pivot})^{\beta_L}$ to the estimated halo masses as described in VU11, with $L_{\rm pivot} = 10^{11}\ L_{r',\odot}$.

This relation we then use to assign halo masses to our lenses. Constructing NFW haloes from these halo masses at the photometric redshift of the lenses, we create mock source catalogues with the observed source redshift distribution but with simulated shear estimates with strengths corresponding to those which would be induced by our lens haloes. Finally we measure the mock signal within 200 h^{-1} kpc of the lenses in each luminosity bin and take this to be the 'true' signal. We only use the small scales for our mass estimate to avoid complications due to insufficient treatment of clustering, and we force our satellite fraction to zero to obtain a pure NFW fit. Scattering the lenses, assuming a Gaussian error distribution of width $\Delta z = (0.004 m_{i'} - 0.04)(1 + z)$ (see Hildebrandt et al. (2012) for a plot of the photometric redshift errors as a function of magnitude), we then measure the signal in each of 10 realisations and compare the resulting estimated halo masses to the 'true' halo masses. The average of these realisations provides the observed halo mass given the bias, with errors equal to the standard deviation. Since the starting point is a perfect signal, the number of realisations given the area is adequate to retrieve the bias.

The results from this test are shown in Figure 4.9. The quality of our photometric redshifts is high which means that the correction factor is small overall, reaching only $\sim 15\%$ for a luminosity of $L_{r'} \sim 2.5 \times 10^{11}\ L_{\odot}$. Here the contamination is largest due to the shape of the luminosity function causing a larger fraction of low luminosity objects to scatter into the higher-luminosity bin. For our faintest red luminosity bin the correction is $\sim 10\%$, in this case caused by larger errors in the photometric redshift estimates. The correction factor is less than unity for lower-luminosity bins due to the turn-over of the distribution of red lenses at $M_{r'} \sim -21.2$ (see Figure 4.5). The small correction factor for blue lenses is due to their flatter mass-luminosity relation (see Figure 4.10). Because of the relative insensitivity of halo mass to changes in luminosity, minor errors in luminosity measurements due to photometric redshift inaccuracies will not strongly affect the halo mass estimate. The process described in this section could in principle be iterated over, starting from the fitting of a mass-luminosity relation, until convergence is reached. Since Hoekstra et al. (2005) find that different choices for that relation yield similar curves, we choose not to iterate further.

4.5.2 Luminosity scaling relations

The estimated halo masses for all luminosity bins, corrected for bias due to errors in the photometric redshifts, are shown as a function of luminosity in the top panel of Figure 4.10. Red lenses display a steeper relationship between halo mass and luminosity than blue lenses do, and the higher luminosity bins contain too few blue lenses to adequately constrain the mass. As done in VU11, we fit a powerlaw of the form $M_{200} = M_{0,L}(L/L_{\rm pivot})^{\beta_L}$ to our lensing signal, with $L_{\rm pivot} = 10^{11} L_{r',\odot}$. Rather than fitting to the final mass estimates we fit this relation directly to the lensing signals themselves. We do this because the error bars are asymmetric in the former case, making a fit more complicated. The difference in results between the two fitting techniques is small however.

For our red lenses we find $M_{0,L} = 3.53^{+0.29}_{-0.29} \times 10^{12}\ h^{-1}\ M_{\odot}$ and $\beta_L = 1.28^{+0.10}_{-0.08}$, while for our blue lenses the corresponding numbers are $M_{0,L} = 3.45^{+0.98}_{-1.47} \times 10^{11}\ h^{-1}\ M_{\odot}$ and $\beta_L = 0.50^{+0.18}_{-0.12}$. The constraints for these fits

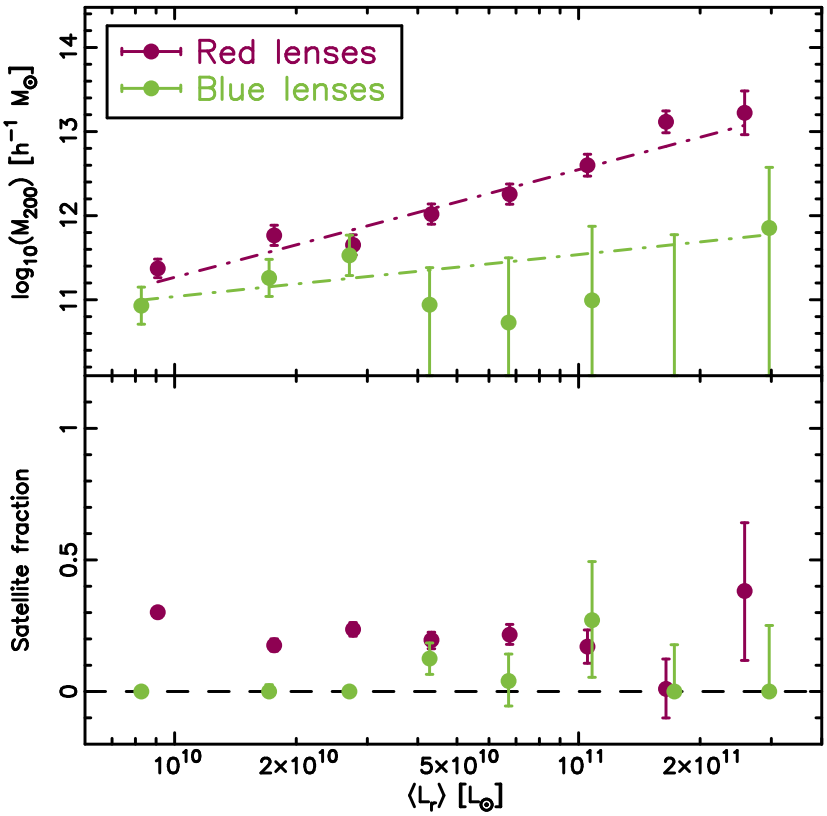

Figure 4.10 Satellite fraction α and bias-corrected halo mass M_{200} as a function of r'-band luminosity. Purple (green) dots represent the results for red (blue) lens galaxies, and the dash-dotted lines show the powerlaw scaling relations as described in the text.

are shown in Figure 4.11. Here we again see that the red lenses are better constrained than the blue. This is partly because we have more red lenses, and partly because red lenses in general are more massive making the lensing signal stronger. Our powerlaws are shallower than the ones found by VU11, but there are some differences between the analyses, making a direct comparison difficult. The way we select our red and blue samples differs significantly from the VU11 selection of early- and late-type samples (which is based on estimated Sérsic profiles rather than colours). Furthermore, in our halo model we account for the baryonic mass of each lens, something that was not done in VU11. Removing the baryonic component from our model, we find that the masses for some bins are overestimated by as much as 60%. It may appear counter-intuitive that including a baryonic component with a mass which is of order 10% of the total mass should result in such a significantly lowered halo mass estimate. The explanation lies in the halo model fitting, and specifically in the way the satellite fraction is allowed to vary. Adding a baryonic component on small scales will result in a lowered central halo mass. The central halo profile reaches further than the baryonic component however, and thus power on intermediate

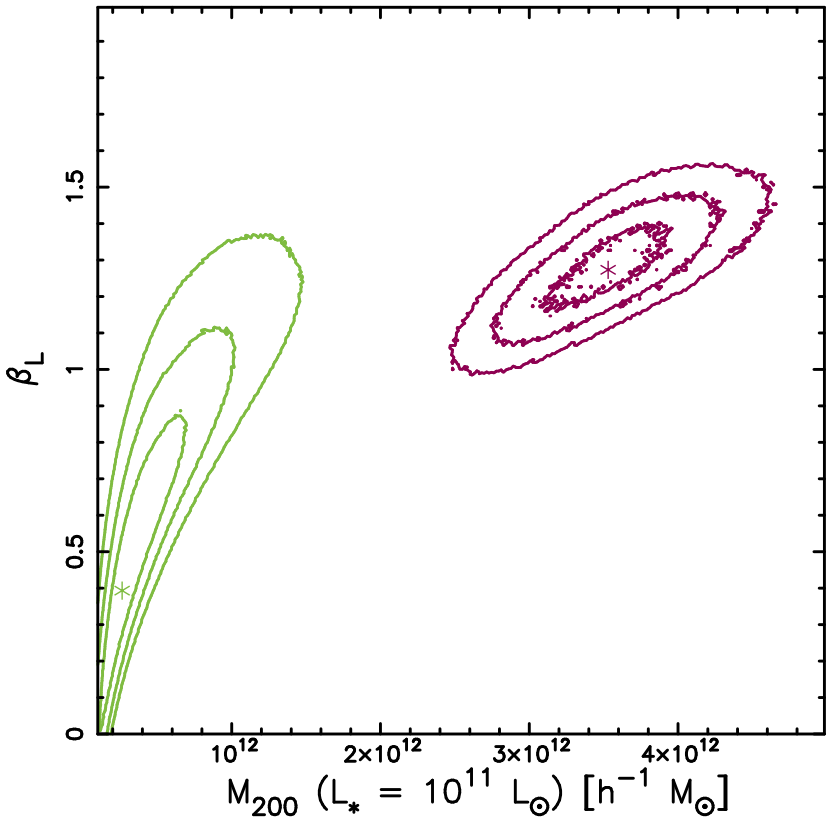

Figure 4.11 Constraints on the powerlaw fits shown in Figure 4.10. In purple (green) we show the constraints on the fit for red (blue) lenses, with lines representing the 67.8%, 95.4% and 99.7% confidence limits and stars representing the best-fit value.

scales is also diminished. To compensate for this loss of power, the halo model will increase the satellite 1-halo term by increasing the satellite fraction, which also increases the stripped satellite halo term, lowering the central 1-halo term further until an equilibrium is reached. These mechanisms are illustrated for red galaxies in luminosity bin L4 in Figure 4.12, where we have allowed halo mass, satellite fraction and stellar mass fraction to vary simultaneously for both panels. This Figure also makes clear the degeneracies introduced to the halo model if the stellar mass is left as a free parameter.

Higher-luminosity bins are more severely affected by this effect than the lower-luminosity end due to the lack of a prominent satellite 1-halo feature. The net effect is a steeper slope, which is exactly what VU11 are displaying. The general overestimation of halo mass in VU11 also means that the mass of a $L = 10^{11} L_{r',\odot}$ galaxy is overestimated, partly explaining the discrepancy between the $M_{0,L}$ estimates.

VU11 also convert their best-fit halo masses to mean halo masses, accounting for the fact that the halo mass function is a declining function, causing us to preferentially pick lower-mass haloes. The lensing best-fit halo mass therefore

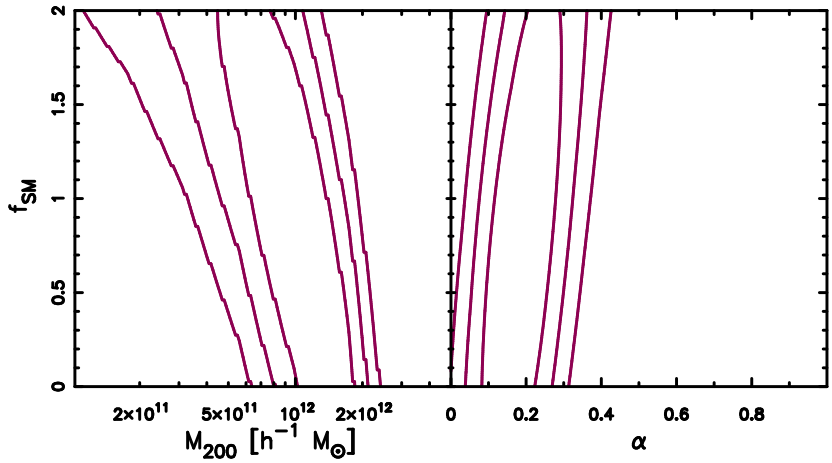

Figure 4.12 Dependence of halo model fitting parameters halo mass M_{200} and satellite fraction α on stellar mass, with $f_{\rm SM}$ the fraction of true mean stellar mass used in the halo model and contours showing the 67.8%, 95.4% and 99.7% confidence intervals. The left panel shows that including a baryonic component in the model (i.e. setting $f_{\rm SM} = 1$) will result in a significantly lower best-fit halo mass than not doing so ($f_{\rm SM} = 0$), and the right panel shows that the reason for this is an increased satellite fraction.

does not correspond to the mean halo mass in a given bin. The correction factors they apply range between a few percent for the lower-luminosity bins to $\sim 30\%$ at the highest luminosities.

Another important factor to take into account is the fact that we limit our lens samples to redshifts of $0.2 < z_{\rm lens} < 0.4$ keeping our mean lens redshift fairly stable at $\langle z_{\rm lens} \rangle \sim 0.3$. This is not done in VU11 and as a result, the median redshift of our lower-luminosity bins is higher than for the same bins in VU11, with the opposite being true for the higher-luminosity bins. Recent numerical simulations indicate that the relation between stellar mass and halo mass will evolve with redshift (e.g. Conroy & Wechsler, 2009; Moster et al., 2010). Lower-mass host galaxies ($M_* < 10^{11}\ M_\odot$) increase in stellar mass faster than their halo mass increases, i.e. for higher redshifts the halo mass is lower for the same stellar mass. The opposite trend holds for higher-mass host galaxies ($M_* > 10^{11}\ M_\odot$). As a result, the relation between halo mass and stellar mass (or an indicator thereof, such as luminosity) steepens with increasing redshift. This means that for the lower-luminosity bins, where our redshifts are higher, we may measure a steeper slope than VU11 and vice-versa for higher-luminosity bins. There are other factors which could affect the measured slope, such as the scatter between luminosity bins due to errors in the estimated luminosities. VU11 find that this bias is only relevant for the two highest luminosity bins, and that the correction factor is small compared to the error on the halo mass. We therefore choose not to model this effect in this Chapter.

4.5.3 Satellite fraction

The lower panel of Figure 4.10 shows the satellite fraction α as a function of luminosity for both the red and the blue sample. At lower luminosities the satellite fraction is $\sim 40\%$ for red lenses and as luminosity increases the satellite fraction decreases. This indicates that a large number of faint red lenses are satellites inside a larger dark matter halo, consistent with previous findings (e.g. Mandelbaum et al., 2006b; van Uitert et al., 2011). In the highest luminosity bins the satellite fraction is difficult to constrain due to the shape of the halo model satellite terms (green lines in Figure 4.2) becoming indistinguishable from the central 1-halo term (purple dashed), as discussed in Appendix 4.A. For blue lenses, the satellite fraction remains low across all luminosities indicating that almost none of our blue galaxies are satellites, again consistent with previous findings. This may be a sign that blue galaxies in our analysis are in general more isolated than red ones, a theory corroborated by the low signal on large scales for blue galaxies (see Figure 4.20 in Appendix 4.A). Here we have made no distinction between field galaxies and galaxies residing in a more clustered environment.

4.6 Stellar mass trend

A more accurate indicator of the baryonic content of a galaxy than its luminosity is its stellar mass, since luminosity is sensitive to recent star formation. We therefore study the relation between stellar mass and the dark matter content in this Section, dividing the lenses into 9 stellar mass bins as illustrated in Figure 4.13 with details in Table 4.3. As in Section 4.5 we further split each stellar mass bin into a red and a blue sample using their photometric types to approximate early- and late-type galaxies.

We measure the galaxy-galaxy lensing signal for each sample as before, and fit using our halo model with the halo mass M_{200} and the satellite fraction α as free parameters. Similarly to the previous section, the results are shown in Figure 4.14 for all stellar mass bins and for each red and blue lens sample, with details of the fitted halo model parameters quoted in Table 4.3. In the case of blue lenses, the two highest stellar mass bins are not well-constrained, due to a lack of lenses, and we therefore remove them from our analysis. The same issues with a direct comparison between this analysis and the one presented in VU11 remain: (1) their halo masses are likely overestimated due to inadequate modelling of the baryonic component, (2) our red and blue samples do not necessarily correspond to their early- and late-type galaxies, (3) we limit our analysis to a narrow redshift range of $0.2 < z_{\rm lens} < 0.4$ and (4) we have photometric redshifts for all our objects while VU11 had access to spectroscopic redshifts but for their lenses only. The latter effect we again account for in a similar fashion to the procedure described in Section 4.5.1.

An overview of the trends in Figure 4.14 is given in Figure 4.15 for red lenses and Figure 4.16 for blue. The mean mass in each bin increases with increasing stellar mass as expected, resulting in an increased signal amplitude. Similar to what we saw in the luminosity samples in the previous Section, the lower-mass bins display a bump at scales of $\sim 0.5\ h^{-1}$ Mpc. Here the lowest bins contain less massive galaxies than the lowest luminosity bins and the bump is more

Table 4.3 Details of the stellar mass bins. (1) Stellar mass range [$M_\odot$]; (2) Number of lenses; (3) Mean redshift; (4) Fraction of lenses that are blue; (5) Mean luminosity for red lenses [10^{10} $L_\odot$]; (6) Mean stellar mass for red lenses [10^{10} $M_\odot$]; (7) Best-fit mean halo mass for red lenses [10^{11} h^{-1} $M_\odot$]; (8) Best-fit satellite fraction for red lenses; (9) Mean luminosity for blue lenses [10^{10} $L_\odot$]; (10) Mean stellar mass for blue lenses [10^{10} $M_\odot$]; (11) Best-fit mean halo mass for blue lenses [10^{11} h^{-1} $M_\odot$]; (12) Best-fit satellite fraction for blue lenses

Sample	$\log_{10} M_*{}^{(1)}$	$n_{\rm lens}{}^{(2)}$	$\langle z\rangle^{(3)}$	$f_{\rm blue}{}^{(4)}$	$\langle L_r^{\rm red}\rangle^{(5)}$	$\langle M_*^{\rm red}\rangle^{(6)}$	$M_h^{\rm red(7)}$	$\alpha^{\rm red(8)}$	$\langle L_r^{\rm blue}\rangle^{(9)}$	$\langle M_*^{\rm blue}\rangle^{(10)}$	$M_h^{\rm blue(11)}$	$\alpha^{\rm blue(12)}$
S1	[9.00,9.50]	399730	0.29	0.88	0.04	0.20	$0.01^{+0.01}_{-0.00}$	$0.53^{+0.02}_{-0.03}$	0.06	0.18	$0.35^{+0.10}_{-0.14}$	$0.00^{+0.01}_{-0.00}$
S2	[9.50,10.00]	240732	0.30	0.85	0.11	0.56	$0.07^{+0.04}_{-0.03}$	$0.78^{+0.02}_{-0.02}$	0.19	0.56	$0.50^{+0.14}_{-0.20}$	$0.02^{+0.01}_{-0.01}$
S3	[10.00,10.50]	146657	0.30	0.73	0.37	1.95	$0.43^{+0.28}_{-0.17}$	$0.58^{+0.02}_{-0.02}$	0.57	1.73	$1.16^{+0.33}_{-0.26}$	$0.00^{+0.01}_{-0.00}$
S4	[10.50,11.00]	91556	0.30	0.39	1.14	6.05	$3.02^{+0.96}_{-0.73}$	$0.26^{+0.01}_{-0.02}$	1.66	5.15	$1.63^{+0.47}_{-0.65}$	$0.00^{+0.01}_{-0.00}$
S5	[11.00,11.25]	26942	0.30	0.15	2.60	13.3	$5.75^{+1.83}_{-1.39}$	$0.21^{+0.02}_{-0.02}$	4.20	12.8	$1.16^{+1.32}_{-0.83}$	$0.11^{+0.05}_{-0.05}$
S6	[11.25,11.50]	13287	0.30	0.07	4.51	23.2	$11.6^{+3.71}_{-2.81}$	$0.20^{+0.03}_{-0.03}$	7.31	22.1	$3.78^{+4.88}_{-2.53}$	$0.10^{+0.09}_{-0.09}$
S7	[11.50,11.75]	4481	0.30	0.04	7.82	40.2	$25.7^{+8.17}_{-6.19}$	$0.25^{+0.03}_{-0.04}$	13.6	40.0	$0.01^{+2.31}_{-0.00}$	$0.00^{+0.22}_{-0.00}$
S8	[11.75,12.00]	890	0.30	0.04	13.5	68.9	$121^{+42.2}_{-31.3}$	$0.26^{+0.07}_{-0.07}$	25.3	72.3	$10.2^{+30.5}_{-10.2}$	$0.15^{+0.36}_{-0.30}$
S9	[12.00,12.50]	147	0.29	0.20	24.5	127	$115^{+40.1}_{-51.8}$	$0.59^{+0.19}_{-0.19}$	51.9	144	$0.01^{+9.86}_{-0.00}$	$0.00^{+0.35}_{-0.00}$

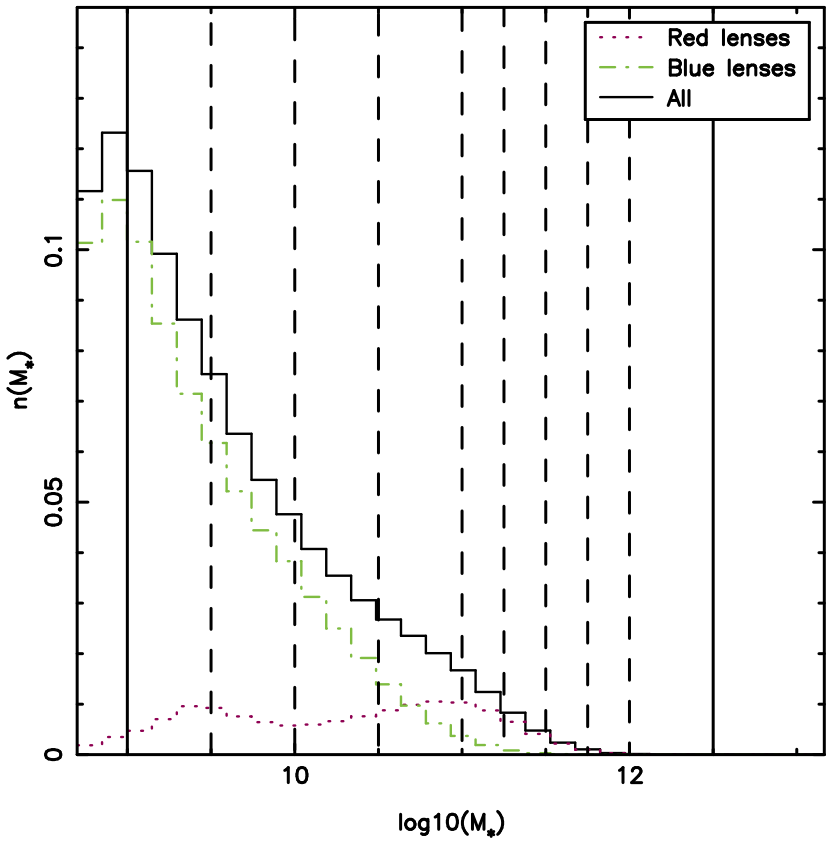

Figure 4.13 Stellar mass distribution in the CFHTLS for lenses with redshifts $0.2 \leq z_{\rm lens} \leq 0.4$ (black solid histogram). The distribution of red (blue) lenses is shown in dotted purple (dot-dashed green). Our lens bins are marked with vertical lines.

pronounced, indicating that most of the galaxies in these low-mass samples are satellite galaxies. The contribution from nearby haloes is again clearly visible in the lower-mass blue samples. The two highest-mass bins contain too few lenses to constrain the signal and have therefore been removed.

4.6.1 Stellar mass scaling relations

The best-fit halo masses and satellite fractions for each stellar mass bin are shown in Figure 4.17. We have corrected the halo masses for the bias induced by errors in our photometric redshift estimates using the mean luminosity in each bin as before. It is clear that the relation between dark matter halo and stellar mass is different for red and blue lenses as expected. To quantify the difference, we fit a powerlaw to the lensing signals in each bin simultaneously, similarly to our treatment of the luminosity bins in the previous Section. The form of the powerlaw is $M_{200} = M_{0,M}(M_*/M_{\rm pivot})^{\beta_M}$ with $M_{\rm pivot} = 2{\times}10^{11}\ M_\odot$ as in VU11. We note here that for the lowest red stellar mass bins, though the halo model fits the data very well (see Figure 4.14), the sample consists of nearly

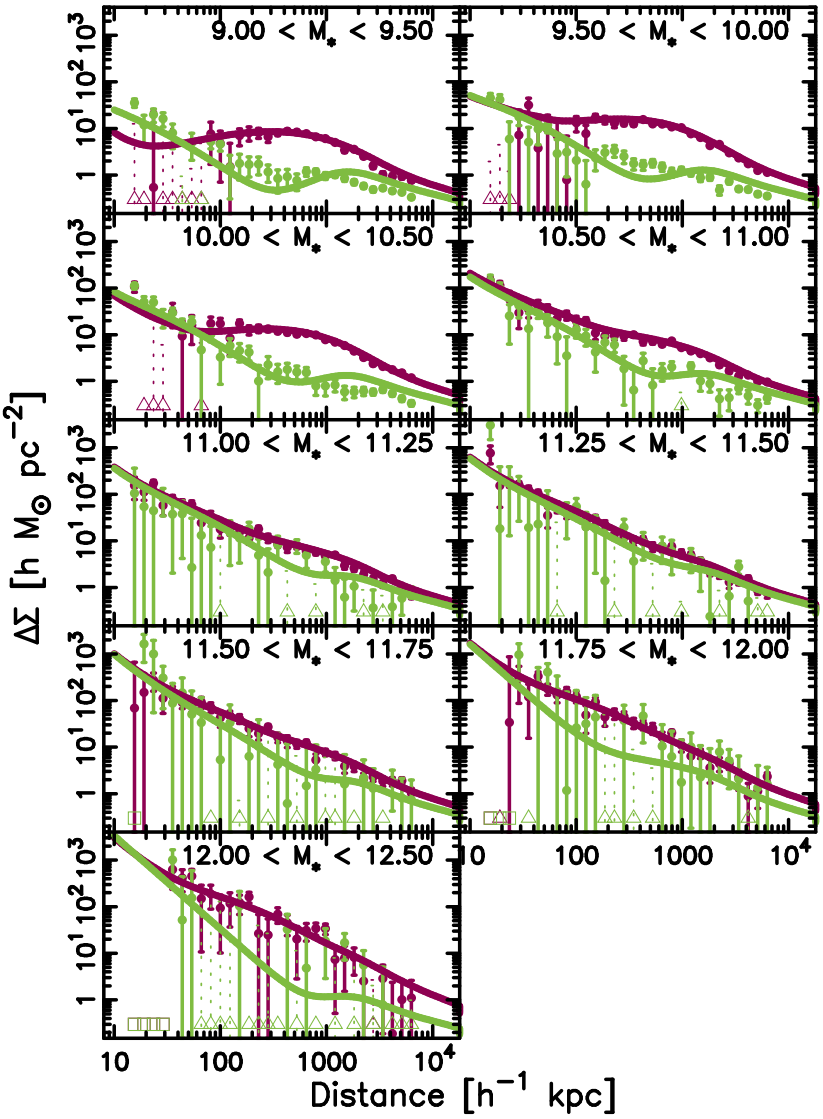

Figure 4.14 The weak galaxy-galaxy signal around lenses which have been split into stellar mass bins according to Table 4.3, modelled using the halo model described in Section 4.3.2. The purple (green) dots represent the measured differential surface density of the red (blue) lenses, and the solid line is the best-fit halo model. Triangles represent negative points that are included unaltered in the model fitting procedure, but that have here been moved up to positive values as a reference. The dotted error bars are the unaltered error bars belonging to the negative points. The squares represent distance bins containing no objects. For a detailed decomposition into the halo model components, please refer to Appendix 4.B.

100% satellite galaxies. It is therefore not a central halo mass associated with these lenses that is constrained by the halo model and so we exclude the two

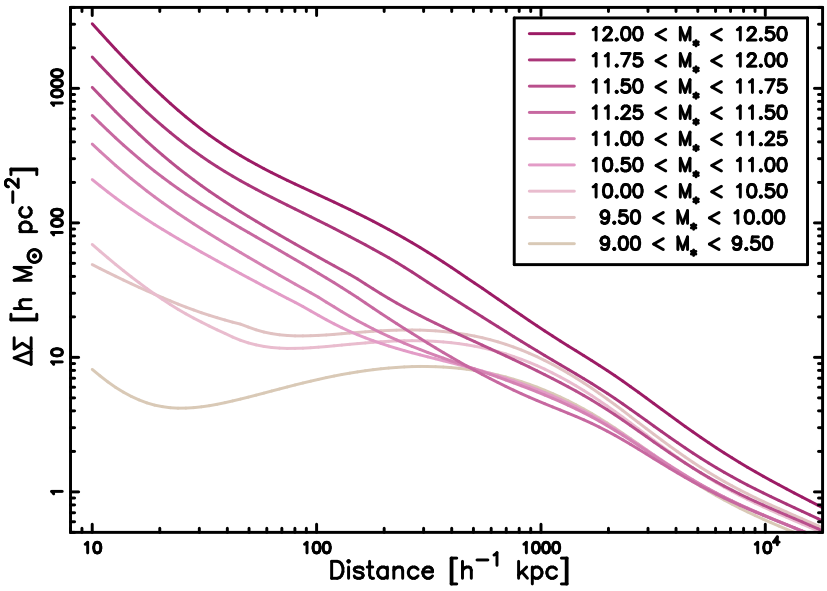

Figure 4.15 Best-fit halo models for red lenses for all stellar mass bins.

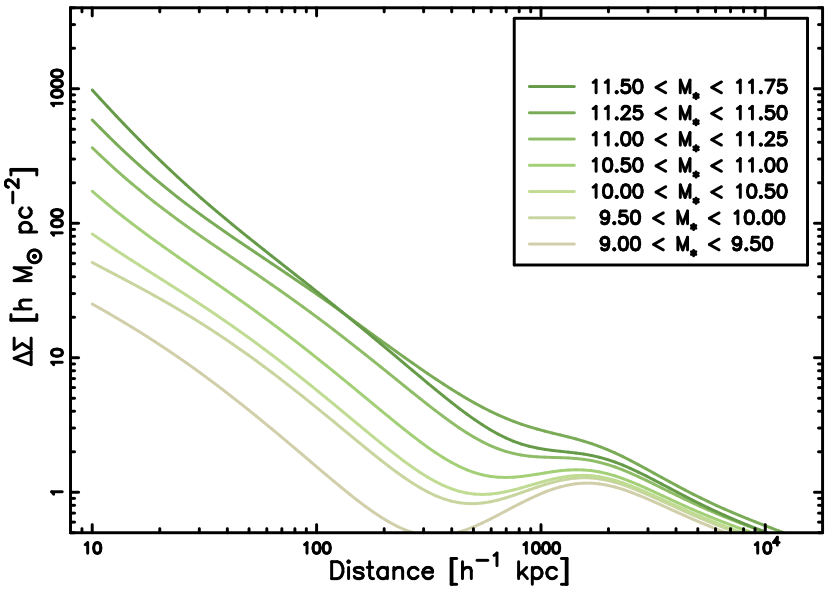

Figure 4.16 Best-fit halo models for blue lenses for all stellar mass bins.

lowest stellar mass bins from our analysis.

The resulting best-fit values for red lenses are $M_{0,M} = 1.07^{+0.10}_{-0.06} \times 10^{12}\ h^{-1}\ M_{\odot}$ and $\beta_M = 1.36^{+0.10}_{-0.06}$, and for blue lenses $M_{0,M} = 3.52^{+0.70}_{-0.70} \times 10^{11}\ h^{-1}\ M_{\odot}$ and $\beta_M = 0.54^{+0.06}_{-0.08}$. We show the constraints and best-fit values in Figure 4.18. The red lenses are clearly better constrained than the blue due to the higher-

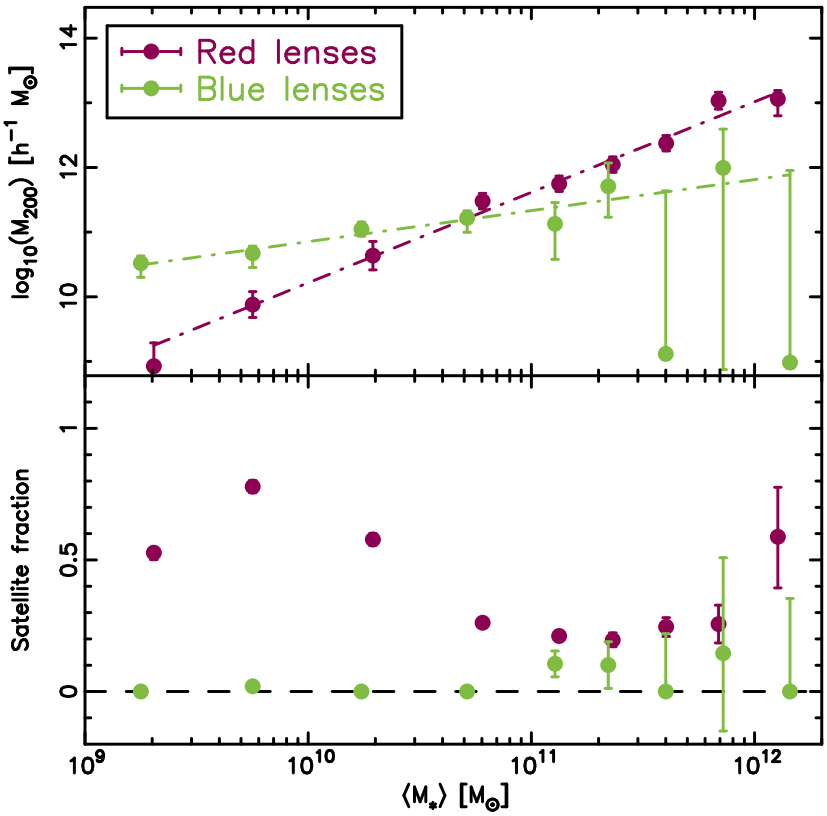

Figure 4.17 Satellite fraction α and halo mass M_{200} as a function of stellar mass. Purple (green) dots represent the results for red (blue) lens galaxies.

quality signal generated by these generally more massive and more abundant galaxies. Similarly to our luminosity relation, this powerlaw is shallower than the one found by VU11 but as discussed in the previous section the two analyses differ in ways that make a direct comparison difficult. Primarily the object selection differs, both in redshift and in defining red and blue lenses, and our halo masses are in general lower since we account for the baryonic mass in the lens while VU11 takes only dark matter into account. This also partly explains the differences in $M_{0,M}$. Furthermore, the stellar mass estimates we use here are based on the luminosity-stellar mass relations derived in Bell et al. (2003). It has since emerged that these relations tend to significantly overestimate the stellar mass (Zibetti et al., 2009). The accuracy of our stellar masses is thus somewhat limited, and new estimates will be derived in the near future using the Zibetti et al. (2009) relations instead.

An effect VU11 does account for, however, is the scatter between mass bins due to inaccuracies in the stellar mass estimate. Due to the shape of the mass distribution (see Figure 4.13), objects will preferentially scatter from lower-mass to higher-mass bins, biasing our halo masses low. The effect is greatest at the highest mass end since the distribution tapers off there and as a result fractionally more low-mass objects will scatter into the higher-mass bin. For

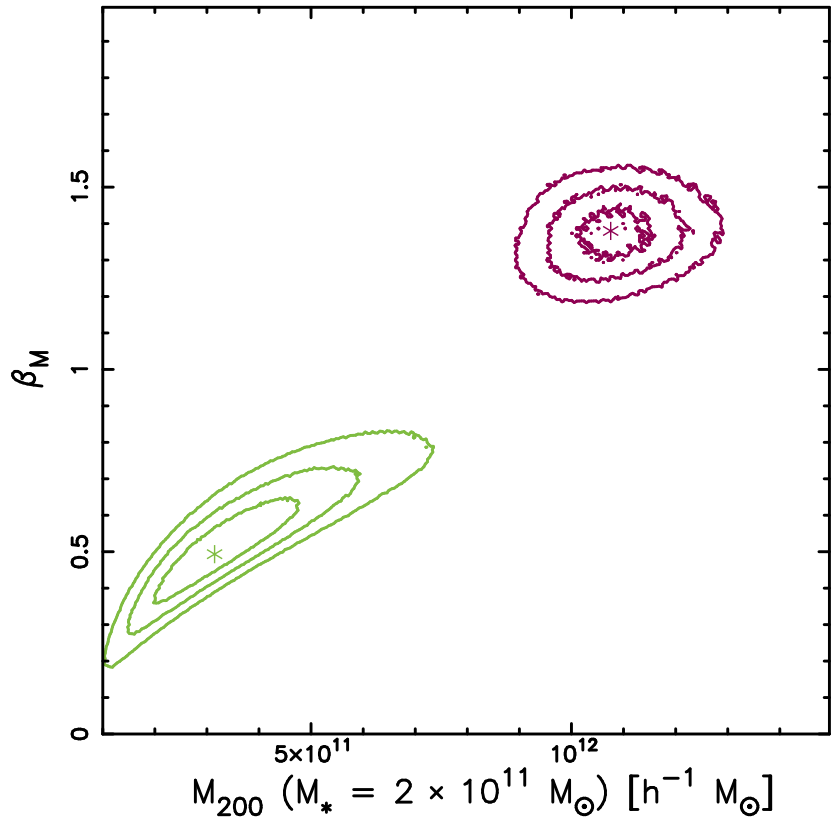

Figure 4.18 Constraints on the powerlaw fits shown in Figure 4.17. In purple (green) we show the constraints on the fit for red (blue) lenses, with lines representing the 67.8%, 95.4% and 99.7% confidence limits and stars representing the best-fit value.

their late-type galaxies, roughly corresponding to our blue sample, VU11 applies a correction of up to 20%, while for their early-type galaxies the correction is $\sim 10\%$ at the low-mass end and reaches $\sim 40\%$ for higher stellar masses. Just as for the luminosity results, they also convert their best-fit halo mass to mean halo mass with corrections of up to $\sim 30\%$ for the highest stellar masses. As a result, their halo mass relation is steepened compared to the uncorrected case, but this is not enough to explain the differences with our results.

The satellite fraction α as a function of stellar mass is shown in the lower panel of Figure 4.17 for both red and blue lenses. In the lower-mass red bins, nearly all lenses are satellites while for higher masses, nearly all are located centrally in their halo as expected. As discussed in the previous section, this fraction is difficult to constrain for high masses due to the shape of the satellite terms. The overall low satellite fraction for blue galaxies, suggesting together with low large-scale signal that most blue galaxies are isolated, is consistent with the luminosity results.

4.7 Discussion and conclusions

In this Chapter we have used high-quality weak lensing data from the CFHTLS to place constraints on the relation between dark matter halo mass and the baryonic content of the lenses, quantified through luminosity and stellar mass estimates. We verified the fidelity of our shear catalogue by comparing our lensing signal with that of two independent shear catalogues, and by using a method based on seeing variations in the data. The impressive source number density in this survey has made it possible to achieve tighter constraints than have so far been attained using previous lensing surveys such as the SDSS or the RCS2. Splitting our lens samples into red and blue subsamples, we approximated the trends for early- and late-type galaxies separately. We also extended our study to lower stellar masses than have been studied before using a halo model such as the one described in this Chapter. We note, however, that the stellar mass estimates used in this analysis are somewhat outdated, which may affect the trends found. In the near future this will be remedied.

As luminosity and stellar mass increases, the halo mass increases as well. For red lenses, the halo mass increases with greater baryonic content at a higher rate than for blue galaxies, independent of whether the measure of baryonic content is luminosity or stellar mass. The two measures thus produce consistent results. For each we fit powerlaw relations to quantify the rate of increase in halo mass. We find that for red galaxies, the halo mass scales with luminosity as $M_{200} \propto L_{r'}^{1.28^{+0.10}_{-0.08}}$ and with stellar mass as $M_{200} \propto M_*^{1.36^{+0.10}_{-0.06}}$, while for blue galaxies $M_{200} \propto L_{r'}^{0.50^{+0.18}_{-0.12}}$ and $M_{200} \propto M_*^{0.54^{+0.06}_{-0.08}}$. For a fiducial red galaxy with a luminosity of $L_0 = 10^{11}\ L_{r',\odot}$ we find a halo mass of $M_{200} = 3.53^{+0.29}_{-0.29} \times 10^{12}\ h^{-1}\ M_\odot$. This number is lower than the number found by VU11, but the two analyses differ significantly in object selection. Furthermore, in this chapter we have included a component of our halo model which was neglected by VU11: the baryonic component. Since the lensing signal is a response to the total mass of a system, it is essential to account for baryons in order to not overestimate the mass contained in the dark matter halo. However, we also showed that great care has to be taken when including a baryonic component since doing so has a greater impact on the fitted halo mass than one might naïvely expect due to the complicated interplay between stellar mass, satellite fraction and halo mass.

For our blue galaxy selection, the satellite fraction is low across all luminosities and stellar masses considered here. The signal at large scales for these samples is also generally low, indicating that these galaxies are relatively isolated and reside in less clustered environments than the red galaxies do and that we may be overestimating the bias for these samples. At low luminosity/stellar mass, a considerable fraction of red galaxies are satellites within a larger dark matter halo. This fraction decreases steadily with increasing luminosity or stellar mass.

The tight constraints on the relation between baryonic content indicators and dark matter halo mass achieved in this work will help improve our understanding of the mechanisms behind galaxy formation. If the halo mass threshold for galaxy formation is accurately known for all galaxies then cosmological simulations can be further improved and phenomena such as the missing satellite problem may be better studied. Furthermore, by studying red and blue lenses

separately we have determined that the bias description which works well for red galaxies is not optimal for blue galaxies. The environments the two samples reside in are thus radically different and the difference will have to be taken into account in the future.

With currently ongoing (e.g. KiDS) and planned (e.g. Euclid) surveys, weak lensing analyses will become yet more powerful than the one presented in this Chapter. In preparation for the future there are therefore several sources of uncertainty that should be investigated. As mentioned above, the bias description may not be optimal for blue lenses and with future data this bias can likely be constrained directly using galaxy-galaxy observations. Recent simulations have also indicated that there is a redshift evolution of the halo mass relations, and this evolution can be studied with weak lensing. Other possible improvements to the halo model used here include studies of the distribution of satellites within a galaxy dark matter halo, and investigations of the stripping of satellite haloes. The analysis presented in this Chapter is already a great improvement on recent analyses, and with future surveys we will be able to use galaxy-galaxy lensing to study the connection between baryons and dark matter in exquisite detail.

Acknowledgements

This Chapter is based on observations obtained with MegaPrime/MegaCam, a joint project of CFHT and CEA/DAPNIA, at the Canada-France-Hawaii Telescope (CFHT) which is operated by the National Research Council (NRC) of Canada, the Institut National des Science de l'Univers of the Centre National de la Recherche Scientifique (CNRS) of France, and the University of Hawaii. This work is based in part on data products produced at TERAPIX and the Canadian Astronomy Data Centre as part of the Canada-France-Hawaii Telescope Legacy Survey, a collaborative project of NRC and CNRS.

MV acknowledges support from the European DUEL Research-Training Network (MRTN-CT-2006-036133) and from the Netherlands Organization for Scientific Research (NWO).

APPENDIX 4.A: Detailed luminosity bins

In this Appendix we show the decomposition of the best-fit halo model for red (Figure 4.19) and blue (Figure 4.20) lenses, split in luminosity according to Table 4.2. Showing the full decomposition is highly informative because it highlights some of the major trends and clarifies which effects dominate in each case.

The baryonic component based on the mean stellar mass in each bin (purple dot-dashed line) becomes more dominant for higher luminosities, but the luminous size of the lenses also increases, making measurement of background source shapes in the innermost distance bins difficult. Thus it is not possible to reliably constrain the baryonic component with our data. Never the less, the effect of including the baryons in our model is an overall lowering of the dark matter halo profile (purple dashed) compared to without baryons. For the red lenses we see that a considerable fraction of the sample at lower luminosities necessarily consists of satellite galaxies, since there is a clear bump in the signal at intermediate scales which has to be accounted for. This satellite fraction continuously drops as luminosity increases, and simultaneously becomes more difficult to constrain since the combination of the stripped satellite profile (green dash-dotted) and satellite 1-halo terms (green dashed) becomes almost indistinguishable from a single NFW profile for high halo masses. This effect was discussed in more detail in VU11, Appendix C.

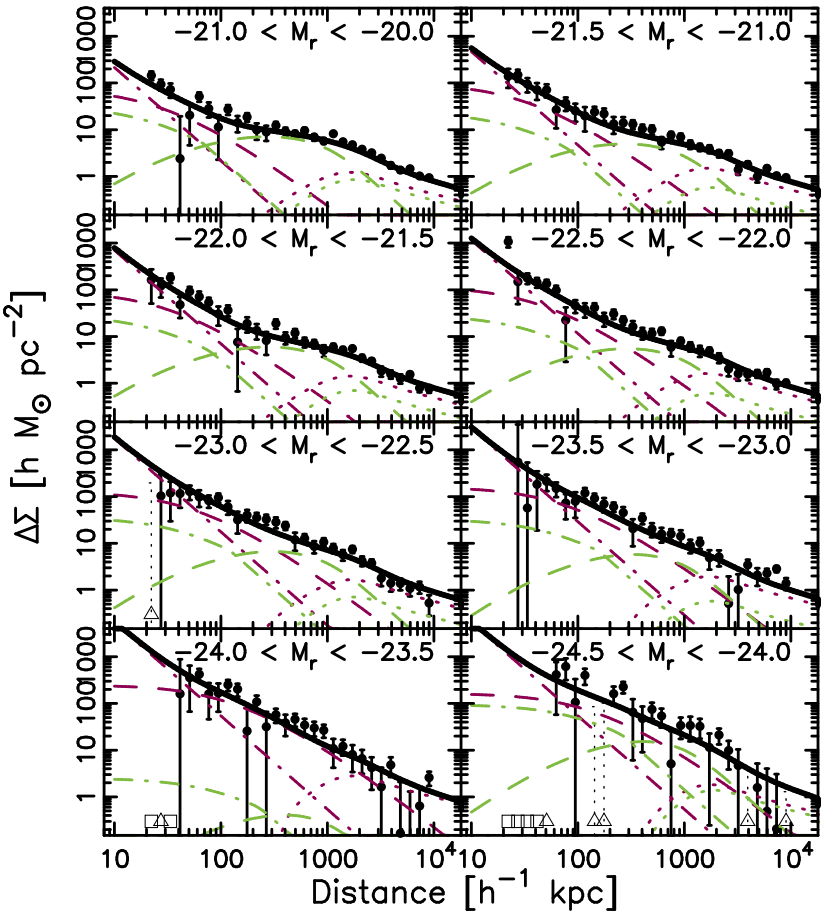

Figure 4.19 The weak galaxy-galaxy signal around *red* lenses which have been split into luminosity bins according to Table 4.2, and modelled using the halo model described in Section 4.3.2. The black dots are the measured differential surface density, and the black line is the best-fit halo model with the separate components displayed using the same convention as in Figure 4.2. Grey triangles represent negative points that are included unaltered in the model fitting procedure, but that have here been moved up to positive values as a reference. The dotted error bars are the unaltered error bars belonging to the negative points. The grey squares represent distance bins containing no objects.

For the blue lenses, the signal becomes very noisy for the two highest-luminosity bins due to a lack of lenses. These two bins are therefore discarded from the full analysis in Section 4.5. In general, blue galaxies produce a noisier signal than red galaxies for the same luminosity cuts. This is because blue lenses are in general less massive, and there are fewer of them which results in a weaker signal. We also notice that nearly all blue lenses are galaxies located at the centre of their halo, rather than being satellites. This is consistent with previous findings. It is possible that satellite galaxies in general are redder because they have been stripped of their gas and thus have had their star formation quenched. It could also mean that most blue galaxies in our analysis

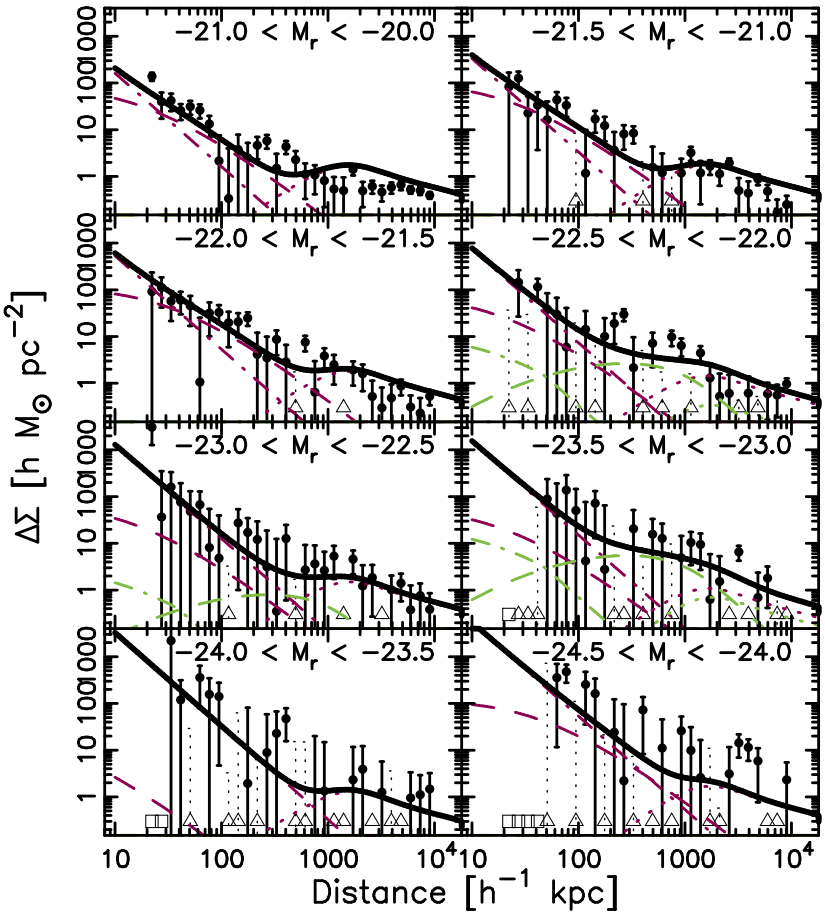

Figure 4.20 The weak galaxy-galaxy signal around *blue* lenses which have been split into luminosity bins according to Table 4.2, and modelled using the halo model described in Section 4.3.2. The black dots are the measured differential surface density, and the black line is the best-fit halo model with the separate components displayed using the same convention as in Figure 4.2. Grey triangles represent negative points that are included unaltered in the model fitting procedure, but that have here been moved up to positive values as a reference. The dotted error bars are the unaltered error bars belonging to the negative points. The grey squares represent distance bins containing no objects.

are isolated; we have made no distinction between field galaxies and galaxies in a more clustered environment. If blue galaxies are more isolated than red ones then the contribution from nearby haloes (dotted lines) would also be less. It is clear from Figure 4.20 that the large scales are not optimally fit by our model, and isolation may be one of the reasons since we assume the same mass-bias relation for blue galaxies as for red. With current data it is not possible to constrain the bias as a free parameter, but with future wider surveys this could be done.

APPENDIX 4.B: Detailed stellar mass bins

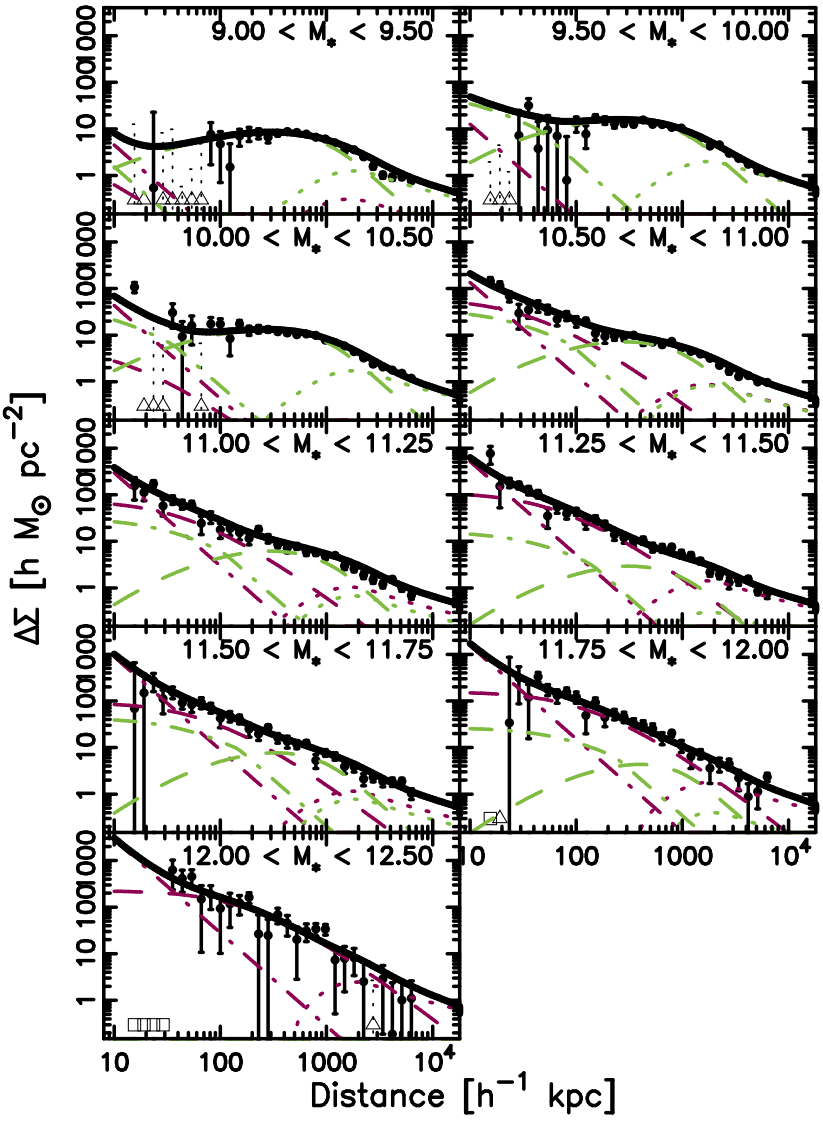

Figure 4.21 The weak galaxy-galaxy signal around *red* lenses which have been split into stellar mass bins according to Table 4.3, and modelled using the halo model described in Section 4.3.2. The black dots are the measured differential surface density, and the black line is the best-fit halo model with the separate components displayed using the same convention as in Figure 4.2. Grey triangles represent negative points that are included unaltered in the model fitting procedure, but that have here been moved up to positive values as a reference. The dotted error bars are the unaltered error bars belonging to the negative points. The grey squares represent distance bins containing no objects.

The decomposition of the best-fit halo model for red and blue lenses, divided

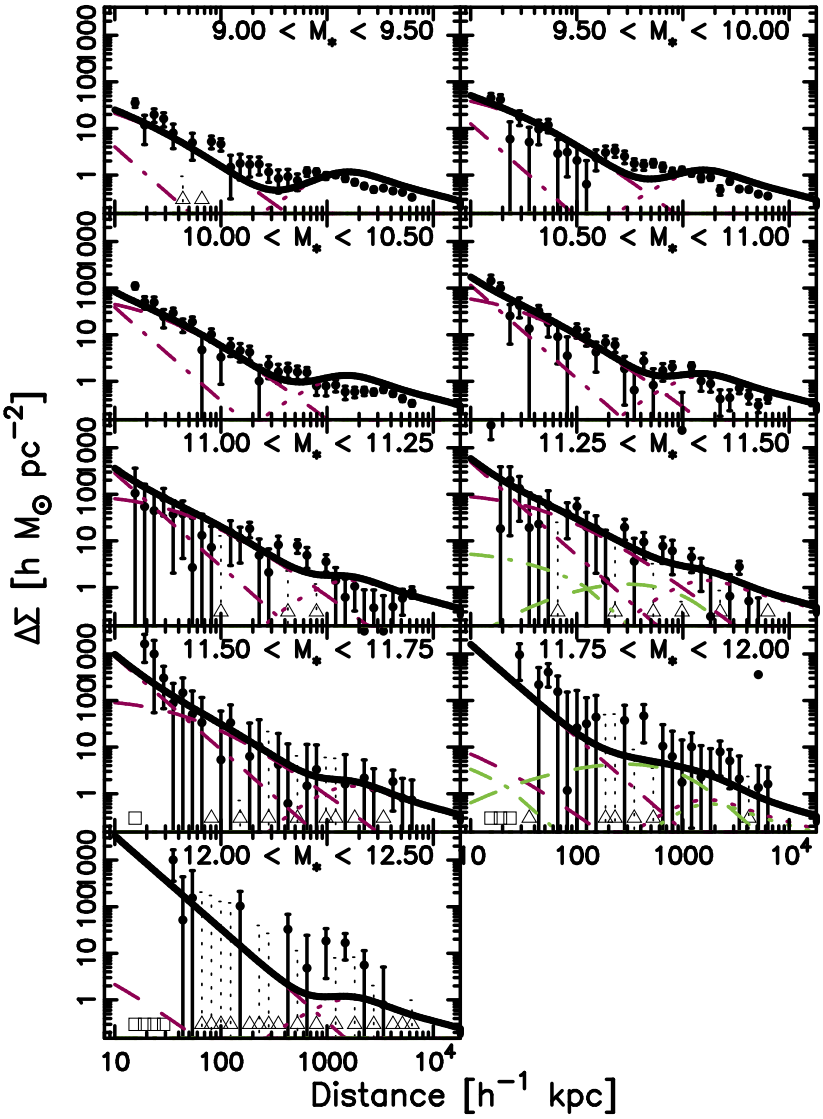

Figure 4.22 The weak galaxy-galaxy signal around *blue* lenses which have been split into stellar mass bins according to Table 4.3, and modelled using the halo model described in Section 4.3.2. The black dots are the measured differential surface density, and the black line is the best-fit halo model with the separate components displayed using the same convention as in Figure 4.2. Grey triangles represent negative points that are included unaltered in the model fitting procedure, but that have here been moved up to positive values as a reference. The dotted error bars are the unaltered error bars belonging to the negative points. The grey squares represent distance bins containing no objects.

using stellar mass as detailed in Table 4.3, is shown in Figures 4.21 and 4.22 respectively.

By construction the baryonic component amplitude (purple dash-dotted line)

increases with increasing bin number, and so does the dark matter halo mass (dashed lines). Note that with our stellar mass selections we push to smaller and fainter objects, so the objects in the three lowest-mass bins are on average less massive and less luminous than the galaxies in the faintest luminosity bin. In these bins, nearly all red galaxies are satellites, while for higher stellar mass bins the satellite fraction diminishes, a behaviour which is consistent with the trends we saw for luminosity (Appendix 4.A). For the higher stellar mass bins, as for the higher luminosity bins, the sum of the satellite stripped and 1-halo terms result in a profile which resembles a single NFW profile, making the satellite fraction more difficult to determine. For the blue lenses we run into the same issues for the highest mass bin as for the highest luminosity bins; the number of lenses is too small to constrain the halo model and so the bin has to be discarded. Furthermore, the satellite fraction is low across all blue lens bins indicating that these lenses are most likely isolated, which is consistent with the low large-scale signal and with our findings for luminosity.